Materials Today Bio 18 (2023) 100542

Contents lists available at ScienceDirect

Materials Today Bio

journal homepage: www.journals.elsevier.com/materials-today-bio

Reduction-responsive worm-like nanoparticles for synergistic cancer chemo-photodynamic therapy

Hang Hu [a,1], Defeng Xu [b,1], Qingbo Xu [c,1], Yuxiang Tang [d,e], Jun Hong [b], Yu Hu [d,e,***], Jianhao Wang [b,**], Xinye Ni [a,*]

[a] Second People's Hospital of Changzhou, Nanjing Medical University, Changzhou, Jiangsu, China
[b] School of Pharmacy, Changzhou University, Changzhou, Jiangsu, China
[c] Guangdong Provincial Key Laboratory of Tumor Interventional Diagnosis and Treatment, Zhuhai Interventional Medical Center, Zhuhai People's Hospital (Zhuhai Hospital Affiliated with Jinan University), Zhuhai, China
[d] Institute of Hematology, Union Hospital, Tongji Medical College, Huazhong University of Science and Technology, Wuhan, China
[e] Hubei Clinical Medical Center of Cell Therapy for Neoplastic Disease, Wuhan, China

ARTICLE INFO

Keywords:
New indocyanine green
Prodrug nanoparticles
Curcumin
Angiogenesis
Photodynamic therapy

ABSTRACT

Chemo-photodynamic therapy shows great potential for cancer treatment. However, the rational integration of chemotherapeutic agents and photosensitizers to construct an intelligent nanoplatform with synergistic therapeutic effect is still a great challenge. In this work, curcumin-loaded reduction-responsive prodrug nanoparticles of new indocyanine green (Cur@IR820-ss-PEG) were developed for synergistic cancer chemo-photodynamic therapy. Cur@IR820-ss-PEG exhibit high drug loading content and special worm-like morphology, contributing to their efficient cellular uptake. Due to the presence of the disulfide bond between IR820 and PEG, Cur@IR820-ss-PEG display reduction responsive drug release behaviors. The efficient cellular uptake and reduction triggered drug release of Cur@IR820-ss-PEG lead to their enhanced in vitro cytotoxicity against 4T1cells as compared to the mixture of IR820 and curcumin (IR820/Cur) under laser irradiation. Besides, Cur@IR820-ss-PEG exhibit prolonged blood half-life time, better tumor accumulation and retention, enhanced tumor hypoxia-inducible factor-1α (HIF-1α) and vascular endothelial cell growth factor (VEGF) suppression effect as compared to IR820/Cur. In vivo antitumor activity study, Cur@IR820-ss-PEG effectively inhibit the tumor angiogenesis, which potentiates the PDT efficacy and leads to the best in vivo antitumor effect of Cur@IR820-ss-PEG. This work provides a novel and relatively simple strategy for synergistic cancer chemo-photodynamic therapy.

1. Introduction

Chemotherapy is a traditional and effective clinical cancer treatment method which uses cytotoxic agents to kill cancer cells. However, chemotherapy is often accompanied by severe side effects and might induce drug resistance after a course of treatment. Photodynamic therapy (PDT) uses reactive oxygen species (ROS) in suit generated by photochemical reaction of photosensitizers to cause damage to cancer cells and blood vessels, showing minimal invasiveness and better tolerance [1,2]. Photodynamic therapy has been exploited to combine with photothermal therapy, immunotherapy and chemotherapy to better suppress tumor progression [3–6]. A combination of chemotherapy and PDT has been reported to exhibit enhanced or synergistic therapeutic effect while reduce side effects and overcome the multidrug resistance of cytotoxic agents [7–14].

Hypoxia is a common feature in most of the solid tumors and leads to resistance to multiple therapies [15–18]. In addition, PDT worsens tumor hypoxia, which might cause the poor prognosis of PDT, especially for patients with advanced malignant tumors [17]. Hypoxia inducible factor-1 (HIF-1), a dimeric protein complex, is the primary transcription factor that responds to hypoxia stress. HIF-1 mediates various signaling pathways involved in cell survival, playing important roles in PDT

* Corresponding author.
** Corresponding author.
*** Corresponding author. Institute of Hematology, Union Hospital, Tongji Medical College, Huazhong University of Science and Technology, Wuhan, China.
E-mail addresses: dr_huyu@126.com (Y. Hu), minuswan@cczu.edu.cn (J. Wang), nxy@njmu.edu.cn (X. Ni).
[1] These three authors contributed equally to this work.

https://doi.org/10.1016/j.mtbio.2023.100542
Received 24 November 2022; Received in revised form 28 December 2022; Accepted 3 January 2023
Available online 4 January 2023

resistance [19,20]. Therefore, inhibition of HIF-1α expression is expected to boost PDT efficacy [21,22].

Curcumin is a major active ingredient of turmeric and exhibits diverse biological activities, such as antitumor, antibacterial and anti-inflammatory activities [23–25]. Many studies have shown that curcumin has significant anti-proliferative and pro-apoptotic effects in a wide range of tumor cell lines [26–29]. In addition, curcumin has also been reported to inhibit hypoxia-induced angiogenesis by down-regulation of HIF-1 activity and subsequent suppression of protein expression of vascular endothelial cell growth factor (VEGF) [30–32]. Therefore, a combination of curcumin and photosensitizers might potentiate the photodynamic therapeutic effect by inhibition of hypoxia-induced angiogenesis, leading to synergistic chemo-photodynamic therapeutic effect. However, curcumin exhibits poor water solubility and low bioavailability while most photosensitizers also exhibit hydrophobicity and poor stability, which require the development of advanced drug delivery systems to deliver curcumin and photosensitizers concomitantly and efficiently to exert their antitumor effect synergistically.

Various strategies, including the use of prodrug amphiphiles and physical encapsulation of drugs within nanocarriers, have been exploited for concomitant delivery of multiple drugs to target tissues and cells [33–35]. Physical encapsulation of drugs within nanocarriers can improve the stability, water solubility and biodistribution of the hydrophobic drugs. However, the low drug-loading capacity, premature drug release in the blood and carrier-related potential toxicities significantly hindered their wide clinical applications [36]. In the last decade, the prodrug amphiphiles have emerged as a new multifunctional nanoplatform for cancer theranostics [37,38]. Various stimuli-responsive prodrug nanoassemblies have been successfully developed for combinational cancer treatment [39–41]. In this work, reduction responsive prodrug of new indocyanine green (IR820-ss-PEG) was synthesized and used for encapsulation of curcumin. The as prepared curcumin-loaded IR820-ss-PEG nanoparticles (Cur@IR820-ss-PEG) were evaluated for chemo-photodynamic combinational therapy. As shown in Scheme 1, Cur@IR820-ss-PEG preferentially accumulate at the tumor site after intravenous injection, which are then efficiently taken up by the tumor cells. Inside the tumor cells, the disulfide bonds of Cur@IR820-ss-PEG are effectively cleaved by high concentration of reducing substances, leading to the simultaneous release of curcumin and IR820. The released curcumin significantly inhibits the tumor angiogenesis by suppression of HIF-1α/VEGF, which enhances the photodynamic therapeutic effect of IR820 and leads to the synergistic chemo-photodynamic therapeutic effect.

2. Materials and methods

2.1. Materials

Methoxy polyethylene glycol carboxylic acid (mPEG-COOH, M.W. 2000), cystamine dihydrochloride (97%), *N*-ethyl-*N*'-(3-dimethylaminopropyl) carbodiimide hydrochloride (EDCI, 98%), 4-dimethylaminopyridine (DMAP, 99%), new indocyanine green (IR820, 80%), curcumin

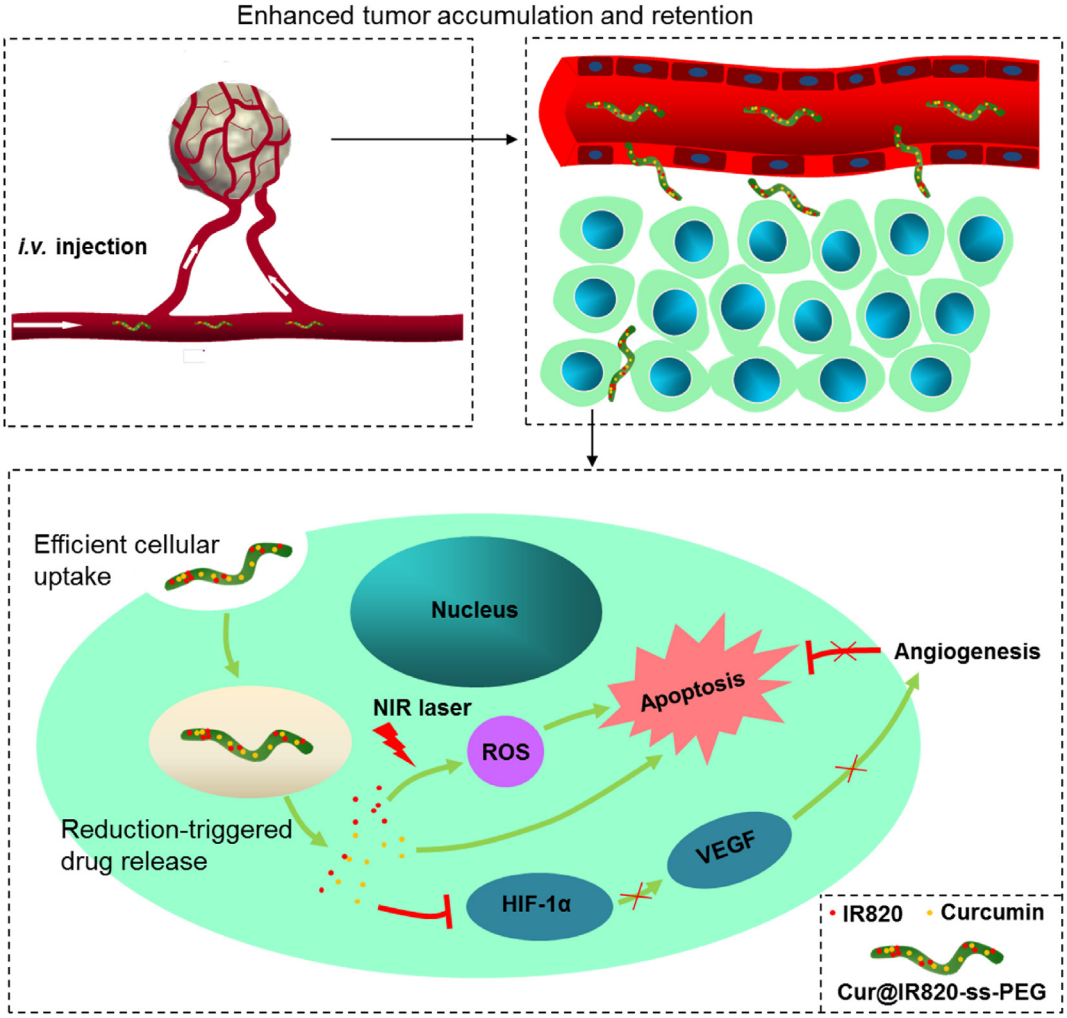

Scheme 1. Schematic illustration of the synergistic antitumor mechanism of Cur@IR820-ss-PEG.

(Cur, 98%), 3-(4,5-dimethylthiazol-2-yl)-2,5-diphenyltetrazolium bromide (MTT), glutathione (GSH, 98%), 1,3-diphenylisobenzofuran (DPBF, 97%) and 2′,7′-dichlorodihydrofluorescein diacetate (DCFH-DA, 97%) were purchased from Aladdin Reagent Co., Ltd (Shanghai, China). All other chemicals were of analytical grade and used as received.

2.2. Synthesis of aminated IR820 (IR820-ss-NH_2)

Briefly, IR820 (170 mg, 0.2 mmol) and cystamine dihydrochloride (450 mg, 2.0 mmol)) were dissolved in 40 mL of methanol. To the solution, triethylamine (606 mg, 6.0 mmol) was added and the resulting mixture was heated to 50 °C and refluxed for 4 h under stirring. Then, the reaction solution was cooled to room temperature, dialyzed against deionized water for 3 days and freeze dried to afford IR820-ss-NH_2 (yield 89%). HRMS (ESI): *m/z* of $[M - Na]^-$ calculated for $C_{50}H_{61}N_4NaO_6S_4$: 941.3479, found: 941.3490.

2.3. Synthesis of IR820-ss-PEG

Briefly, mPEG-COOH (160 mg, 0.08 mmol), EDCI (153 mg, 0.8 mmol), DMAP (20 mg, 0.16 mmol) and IR820-ss-NH_2 (77 mg, 0.08 mmol) were dissolved in 10 mL of *N*, *N*-dimethylformamide. The reaction solution was stirred at room temperature for 24 h. Afterwards, the reaction solution was cooled to room temperature, dialyzed against deionized water for 3 days and freeze dried to afford IR820-ss-PEG (yield 80%).

2.4. Preparation of curcumin-loaded IR820-ss-PEG nanoparticles (Cur@IR820-ss-PEG)

Cur@IR820-ss-PEG was prepared by a thin-film hydration method. In briefly, 50 mg of IR820-ss-PEG and 6 mg of curcumin were added to 50 mL of anhydrous ethanol and stirred overnight at room temperature. Then, the mixture was evaporated under vacuum. The residues were dispersed in 20 mL of deionized water under ultrasonication for 5 min. After that, the dispersion was centrifuged at 8000 rpm for 10 min to remove unencapsulated curcumin. The supernatant was collected and free-dried to obtain Cur@IR820-ss-PEG.

The IR820 and curcumin loading amount were determined by a microplate reader and high-performance liquid chromatography (HPLC), respectively. Briefly, 2 mg of Cur@IR820-ss-PEG powder was dissolved in 2 mL of acetonitrile. The IR820 loading amount was determined by the absorbance at 700 nm using a standard calibration curve. The curcumin loading amount was determined by HPLC using a standard calibration curve. The injection volume was set at 10 μL. The mobile phase consists of acetonitrile and sodium dihydrogen phosphate aqueous solution (0.025 M, pH 3.0) with a volume ratio of 80:20. The detection wavelength was set at 360 nm. The IR820 and curcumin loading content were calculated as:

$$\text{Loading content (IR820)} = \frac{Wt\ (loaded\ IR820)}{Wt\ (drug-loaded\ nanoparticles)} \times 100\% \quad (1)$$

$$\text{Loading content (curcumin)} = \frac{Wt\ (loaded\ curcumin)}{Wt\ (drug-loaded\ nanoparticles)} \times 100\% \quad (2)$$

Where Wt (loaded IR820) is the weight of IR820 loaded in the nanoparticles, Wt (loaded curcumin) is the weight of curcumin loaded in the nanoparticles and Wt (drug-loaded nanoparticles) is the weight of drug-loaded nanoparticles. The loading efficiency of curcumin was calculated as:

$$\text{Loading efficiency (curcumin)} = \frac{Wt\ (loaded\ curcumin)}{Wt\ (added\ curcumin)} \times 100\% \quad (3)$$

Where Wt (added curcumin) is the weight of curcumin added in the preparation of Cur@IR820-ss-PEG.

2.5. Characterization

^{1}H nuclear magnetic resonance (^{1}H NMR) spectra were measured on a NMR spectrometer (AVANCE II 500 MHz, Bruker) using dimethyl sulfoxide-d_6 (DMSO-d_6) as the solvent. The high-resolution mass spectrum (HRMS) was measured on a Q Exactive UHMR Hybrid Quadrupole-Orbitrap Mass Spectrometer (Thermo Scientific). Fourier transform infrared (FT-IR) spectra were measured on a FT-IR spectrometer (iS50, Thermo) by a standard KBr disk method. Ultraviolet–visible (UV–Vis) spectra were measured on a microplate reader (Spark, Tecan). Thermal analysis was performed on a high sensitivity differential scanning calorimeter (DSC, DSC7020, Hitachi) with a closed aluminum pan system over the temperature of 30–300 °C. The DSC analysis was operated at a heating rate of 10 °C/min. The morphologies of the prepared nanoparticles were observed with transmission electron microscope (TEM, JEM-2100, JEOL) operated at an accelerating voltage of 200 KV. To investigate the reduction-responsiveness of the prepared nanoparticles, the nanoparticles were treated with 10 mmol/L of GSH for 24 h and the morphologies were observed with TEM. The samples were negatively stained with 2% phosphotungstic acid (w/w). The size and zeta potential of the prepared nanoparticles were measured by dynamic light scattering (DLS, Nano ZSE, Malvern).

2.6. Dissipative particle dynamics (DPD) simulation

The self-assembly behaviors of IR820-ss-PEG with curcumin in deionized water were studied by PDP simulation. The details of DPD simulation are provided in the supplementary material.

2.7. In vitro singlet oxygen generation

The in vitro singlet oxygen generation was studied by using the singlet oxygen probe DPBF. Briefly, 100 μL of DPBF dimethyl sulfoxide solution (0.4 mg/mL) was added to 1.4 mL of free IR820 or IR820-ss-PEG aqueous solution (24 μg/mL of IR820) and the resulting mixture was immediately irradiated with 0.5 W/cm^2 660 nm laser for 1 min, 2, min, 3 min, 4 min or 5 min. Then, the absorbance at 405 nm was measured by a microplate reader. The experiments were performed in triplicates.

2.8. In vitro drug release

The in vitro drug release behaviors of Cur@IR820-ss-PEG were studied in pH 7.4 PBS buffer (10 mmol/L, 0.5% tween 80), pH 5.0 PBS buffer (10 mmol/L, 0.5% tween 80), pH 7.4 PBS buffer (10 mmol/L, 0.5% tween 80) with 10 mmol/L GSH and pH 5.0 PBS buffer (10 mmol/L, 0.5% tween 80) with 10 mmol/L GSH by using a dialysis method. Briefly, 1 mL of Cur@IR820-ss-PEG was placed into a dialysis tube. The dialysis tube was then immersed in 30 mL of release medium. The release system was shaken at 180 rpm under 37 °C. At 1 h, 2 h, 4 h, 8 h, 12 h, 24 h, 48 h, 72 h and 96 h, 1 mL of release medium was taken out and 1 mL of fresh medium was replenished. The IR820 and curcumin release amount were measured by a microplate reader and HPLC, respectively. The experiments were performed in triplicates in the dark.

2.9. Cell culture

4T1 murine breast cancer cells were cultured in RPMI 1640 medium supplemented with 10% fetal bovine serum, 100 units/mL penicillin and 100 μg/mL streptomycin at 37 °C under 5% carbon dioxide atmosphere.

2.10. Cellular uptake amount

The cellular uptake of IR820/curcumin mixture (IR820/Cur) and Cur@IR820-ss-PEG (24 μg/mL of IR820, 10 μg/mL of curcumin) was observed with fluorescence microscope. In briefly, 4T1 cells were seeded on 12-well plates (1×10^5 cells per well). The cells were treated with IR820/Cur and Cur@IR820-ss-PEG for 2 h or 4 h. After that, the medium was removed and the cells were washed with pH 7.4 PBS buffer for 3 times, fixed with 4% paraformaldehyde and observed with fluorescence microscope.

To determine the intracellular IR820 and curcumin amount, 4T1 cells were seeded on 12-well plates (1×10^5 cells per well) and treated with IR820/Cur and Cur@IR820-ss-PEG (24 μg/mL of IR820, 10 μg/mL of curcumin) for 2 h or 4 h. Then, the medium was removed and the cells were washed with pH 7.4 PBS buffer for 3 times, tripsinized for cell number counting and lysed with 0.5 mL of 1% Triton X-100. The lysates were mixed with 0.5 mL acetonitrile and centrifuged at 10,000 rpm for 10 min. The supernatant was collected and measured by a microplate reader and HPLC to determine the intracellular IR820 amount and curcumin amount, respectively.

2.11. In vitro antitumor effect against 4T1 cells

The in vitro antitumor effect of free curcumin, free IR820, IR820/Cur and Cur@IR820-ss-PEG against 4T1 cells with or without laser irradiation was studied by MTT assays. In brief, 4T1 cells were seeded on 96-well plates (5×10^3 cells per well) and treated with free curcumin, free IR820, IR820/Cur, IR820-ss-PEG and Cur@IR820-ss-PEG with different concentrations for 4 h. Then, the cells were exposed to 0.5 W/cm^2 660 nm laser for 3 min and incubated at 37 °C under 5% carbon dioxide atmosphere for 20 h. The cell viability was determined by a standard MTT assay. To evaluate the cytotoxicity of these formulations against 4T1 cells without laser irradiation, 4T1 cells were treated with these formulations for 24 h and the cell viability was determined by a standard MTT assay.

The morphologies of 4T1 cells after different treatment were also characterized. Briefly, 4T1 cells were seeded on 12-well plates (1×10^5 cells per well) and treated with free curcumin, free IR820, IR820/Cur, IR820-ss-PEG and Cur@IR820-ss-PEG (24 μg/mL of IR820, 10 μg/mL of curcumin) for 4 h. Then, the cells were exposed to 0.5 W/cm^2 660 nm laser for 3 min and incubated at 37 °C under 5% carbon dioxide atmosphere for 20 h. After that, the cells were observed with a microscope.

2.12. Intracellular ROS level

DCFH-DA was used as a fluorescence probe of ROS to determine the intracellular ROS level. In brief, 4T1 cells were seeded on 12-well plates (1×10^5 cells per well). The cells were treated with IR820/Cur and Cur@IR820-ss-PEG (24 μg/mL of IR820, 10 μg/mL of curcumin) for 4 h and DCFH-DA (10 μg/mL) for 20 min. Then, the cells were washed with pH 7.4 PBS buffer for 3 times and exposed to 0.5 W/cm^2 660 nm laser for 3 min. The cellular green fluorescence (2′, 7′-dichlorofluorescein, DCF) generated by the reaction of ROS and DCFH-DA were observed with fluorescence microscope. To determine the intracellular ROS level, the cells were lysed with 0.5 mL of 1% Triton X-100 after laser irradiation. The lysates were centrifuged at 10,000 rpm for 10 min and the fluorescence intensity of the supernatant at 525 nm was determined by a microplate reader (excitation at 485 nm). Cells treated with culture medium alone were used as control.

2.13. In vitro hemolysis assay

In brief, 2 mL of Cur@IR820-ss-PEG with different IR820 concentrations (0.01, 0.05, 0.1, 0.2 and 0.5 mg/mL) in pH 7.4 PBS buffer (10 mM) were mixed with 0.1 mL of 20% red blood cell suspension and the resulting mixture was incubation at 37 °C for 4 h. Afterwards, the mixture was centrifuged at 1000 rpm for 5 min and the absorbance of the supernatant at 540 nm was measured on a microplate reader to determine the hemolysis ratio. 2 mL of deionized water and pH 7.4 PBS buffer were also mixed with 0.1 mL of 20% red blood cell suspension, which were used as positive control and negative control, respectively. The hemolytic ratio was calculated as:

$$\text{Hemolysis}\ (\%) = \frac{Absorbance\ of\ tested\ sample - Absorbance\ of\ negative\ control}{Absorbance\ of\ positive\ control - Absorbance\ of\ negative\ control} \times 100\% \quad (4)$$

2.14. Animal subjects

Female Balb/c mice aged 6–8 weeks were purchased from Hubei Research Center of Experimental Animals. All experimental procedures and the animal use and care protocols were approved by the Animal Care and Use Committee of Huazhong University of Science and Technology.

2.15. Pharmacokinetics

Female Balb/c mice were intravenously administrated with IR820/Cur and Cur@IR820-ss-PEG (18 mg/kg bodyweight as IR820, 7.5 mg/kg bodyweight as curcumin) (n = 3). At 1 min, 5 min, 10 min, 30 min, 1 h, 4 h, 8 h, 12 h and 24 h, the blood samples of mice from each group were collected into heparin treated tubes by removing the mice eyeballs. The plasma samples were obtained by centrifugation at 3000 rpm for 10 min. Then, the obtained plasma samples were extracted by methanol. The IR820 concentration was determined by a microplate reader and the curcumin concentration was determined by HPLC. The pharmacokinetic data were analyzed by Drug and Statistic software version 2.0.

2.16. Biodistribution

Female Balb/c mice were inoculated subcutaneously with 4T1 tumor cells (0.75×10^6) on the right side of the lower back. Tumor-bearing mice were randomly divided into 6 groups (n = 3). IR820/Cur (dissolved in PBS buffer containing 15% dimethyl sulfoxide) and Cur@IR820-ss-PEG (18 mg/kg bodyweight as IR820, 7.5 mg/kg bodyweight as curcumin) were intravenously injected to the corresponding group. Mice were sacrificed 4, 12 and 24 h after intravenous injection. The tumors and main organs including heart, liver, spleen, lung and kidney were excised from the mice. The biodistribution was studied by ex vivo fluorescence imaging in an in vivo imaging system (ABL X5, Tanon).

2.17. HIF-1α/VEGF suppression effect

Tumor-bearing mice were randomly divided into 3 groups (n = 3). pH 7.4 PBS buffer, IR820/Cur (dissolved in PBS buffer containing 15% dimethyl sulfoxide) and Cur@IR820-ss-PEG (18 mg/kg bodyweight as IR820, 7.5 mg/kg bodyweight as curcumin) were intravenously injected to the corresponding group. Mice were sacrificed 24 h after intravenous

injection and the tumors were excised from the mice. The tumor HIF-1α and VEGF expression levels were studied by immunofluorescent staining.

Tumor-bearing mice were randomly divided into 3 groups (n = 3). pH 7.4 PBS buffer, IR820-ss-PEG and Cur@IR820-ss-PEG (18 mg/kg bodyweight as IR820, 7.5 mg/kg bodyweight as curcumin) were intravenously injected to the corresponding group. The tumors of each group were exposed to 0.5 W/cm^2 660 nm laser (3 min) 24 h after intravenous injection. At 48 h, the tumors were excised from the mice. The tumor HIF-1α and VEGF expression levels were studied by immunofluorescent staining.

2.18. In vivo antitumor effect

Female Balb/c mice were inoculated subcutaneously with 4T1 tumor cells (7.5×10^5) on the right side of the lower back. When the 4T1 tumor volumes reached about 160 mm^3, mice were randomly assigned to 5 groups (n = 5) and intravenously injected with each formulation (18 mg/kg bodyweight as IR820, 7.5 mg/kg bodyweight as curcumin). The tumors of each group were exposed to 0.5 W/cm^2 660 nm laser (3 min) 24 h after intravenous injection. At 48 h, the tumor-bearing mice were further intravenously injected with each formulation. The tumors of each group were further exposed to 0.5 W/cm^2 660 nm laser (3 min) at 72 h. Tumor volume and bodyweight of mice from each group were measured every day. At the end of the test, mice from each group were sacrificed. The blood samples were harvested for blood biochemical analysis. The tumors were weighted. The tumor cell density was analyzed by hematoxylin and eosin (H & E) staining. The tumor cell apoptosis was analyzed by TUNEL immunofluorescent staining. The tumor cell proliferation was analyzed by Ki67 immunofluorescent staining. The tumor angiogenesis was analyzed by CD34 immunofluorescent staining. The major organs were also harvested and analyzed by H & E staining.

2.19. Statistical analysis

The data were presented as the means ± standard deviations. The statistical significance of differences between groups was analyzed on Statistical Product and Service Solutions (SPSS) software by independent samples *t*-test. Statistical significance was established at $p < 0.05$.

3. Results and discussion

The synthetic route of IR820-ss-PEG is shown in Fig. 1A. IR820 was first reacted with cystamine to obtain IR820-ss-NH_2 [42]. Then, IR820-ss-NH_2 was condensed with mPEG-COOH in the presence of EDCI and DMAP to afford IR820-ss-PEG. The synthesis of IR820-ss-PEG was characterized ^{1}H NMR, HRMS and FT-IR. The ^{1}H NMR spectrum of IR820-ss-NH_2 shows the characteristic signals of the methylene groups (a) of cystamine (Fig. 1B) compared with IR820 and the HRMS of IR820-ss-NH_2 shows the characteristic signal of $[M - Na]^-$ (Fig. S1), indicating the successful synthesis of IR820-ss-NH_2. The characteristic signals of PEG appear in the ^{1}H NMR spectrum of IR820-ss-PEG compared with IR820-ss-NH_2 (Fig. 1C). The characteristic peak of the C═O stretching vibration of –COOH at 1735 cm^{-1} disappears in the FT-IR spectrum of IR820-ss-PEG compared with mPEG-COOH (Fig. 1D). IR820-ss-PEG exhibits enhanced peak at 1624 cm^{-1} compared with mPEG-COOH and IR820 (Fig. 1D), which is ascribed to the C═O stretching vibration of the newly formed amide bond. These results indicate the successful condensation of mPEG-COOH and IR820-ss-NH_2 through the amide bond. Taken together, these results corroborate the successful preparation of IR820-ss-PEG.

The curcumin-loaded IR820-ss-PEG nanoparticles (Cur@IR820-ss-PEG) were prepared by a thin film-hydration method. Compared with IR820-ss-PEG, Cur@IR820-ss-PEG show enhanced peak at 1590 cm^{-1} and 1513 cm^{-1}, which are correlated to the backbone vibration of the aromatic ring of curcumin, Fig. 1D. The UV–Vis characterization results are shown in Fig. 1E. The absorbance band of IR820-ss-PEG displays blue-shift as compared to free IR820, which is ascribed to the reduced π-conjugation system after substitution of chlorine with amine [42,43]. The characteristic absorbance band of curcumin appears in the UV–Vis spectrum of Cur@IR820-ss-PEG compared with IR820-ss-PEG, indicating the successful loading of curcumin into IR820-ss-PEG nanoparticles. The absorbance band of IR820 in Cur@IR820-ss-PEG exhibits red shift as compared to that in IR820-ss-PEG, which is attributed to the enhanced hydrophobicity of the nanoparticles after loading of curcumin. The thermal analysis results are show in Fig. 1F–I and Fig. S2. Curcumin has an endothermic peak at 186 °C. IR820 exhibits an endothermic peak at 186 °C and an exothermic peak at 247 °C. The DSC thermogram of the prepared IR820-ss-PEG and Cur@IR820-ss-PEG only has the characteristic endothermic peak of PEG and show no characteristic peaks of curcumin or IR820, suggesting that the conjugation of IR820 onto PEG and the encapsulation of curcumin into IR820-ss-PEG nanoparticles significant reduce the degree of crystallization of these two drugs. Collectively, these results confirm the successful preparation of Cur@IR820-ss-PEG.

The drug loading content of curcumin and IR820 was determined by HPLC and a microplate reader, respectively. As shown in Table S1, The IR820 loading content of IR820-ss-PEG is 26.8%. The curcumin loading content and IR820 loading content of Cur@IR820-ss-PEG are 10.2% and 24.5%, respectively. The curcumin loading efficiency of Cur@IR820-ss-PEG is 95%. These results indicate that Cur@IR820-ss-PEG exhibit high drug loading capacity and high drug loading efficiency. The morphology and size of IR820-ss-PEG and Cur@IR820-ss-PEG were characterized by TEM and DLS. As shown in Fig. 2A and B, both IR820-ss-PEG and Cur@IR820-ss-PEG display worm-like morphology and lognormal distribution in hydrodynamic diameters. The hydrodynamic diameters of IR820-ss-PEG and Cur@IR820-ss-PEG are 150.0 ± 3.7 nm and 125.3 ± 4.5 nm, respectively, and both of them have negative zeta potentials, Table S2. To better understand the self-assembly behaviors and structures of Cur@IR820-ss-PEG, DPD simulation was performed [44]. DPD is a coarse-grained simulation method suitable for mesoscale simulation. A whole molecule could be divided into several beads in DPD simulation. Compared to molecular dynamic simulation, DPD simulation significantly reduces the computational load and could realize simulation in larger time and length scales. Besides, DPD simulation maintains enough accuracy as compared to macroscale simulation [45,46]. Fig. S3 shows the definitions of beads and coarse-grained models of IR820-ss-PEG, curcumin and water. Table S3 summarizes the calculated DPD interaction parameters (a_{ij}) between different beads. The DPD simulations were performed in a 100 Å × 100 Å × 100 Å cubic box with periodic boundary conditions, Fig. S4. At the beginning of the simulation, all components are randomly mixed. Fig. 2D shows the representative morphology snapshots at different simulation times, in which the water beads are hidden so as to show the morphology of the aggregate more clearly. As shown in Fig. 2D, IR820-ss-PEG and curcumin aggregate into branched cluster at 0.25 ns. With evolution of the simulation, the branches merge to form dumbbell-like cluster at 0.5 ns. With increasing the simulation time to 20 ns, the dumbbell-like cluster further evolve into a stable worm-like cluster, which is in line with the morphology of Cur@IR820-ss-PEG characterized by TEM, Fig. 2B. It can be seen from the final state of the simulation that there are multiple cores formed by IR820 in the worm-like cluster and curcumin is loaded both in the aggregated PEG chains and cores formed by IR820. Negatively charged IR820 molecules are near to the surfaces of the worm-like cluster, which leads to the negative zeta potential of Cur@IR820-ss-PEG, Table S2.

The in vitro singlet oxygen generation of IR820-ss-PEG was studied using DPBF as a singlet oxygen trapping agent [44,47,48]. As shown in Fig. 2E, both IR820 and IR820-ss-PEG generate singlet oxygen in a time-dependent manner under 0.5 W/cm^2 660 nm laser irradiation. IR820-ss-PEG exhibit slightly enhanced singlet oxygen generation as compared to IR820, which might be ascribed to that the absorbance of IR820-ss-PEG matches better with 660 nm laser. The in vitro drug release behaviors of Cur@IR820-ss-PEG were studied by a dialysis method using GSH as a reducing agent. As shown in Fig. 2F and G, Cur@IR820-ss-PEG

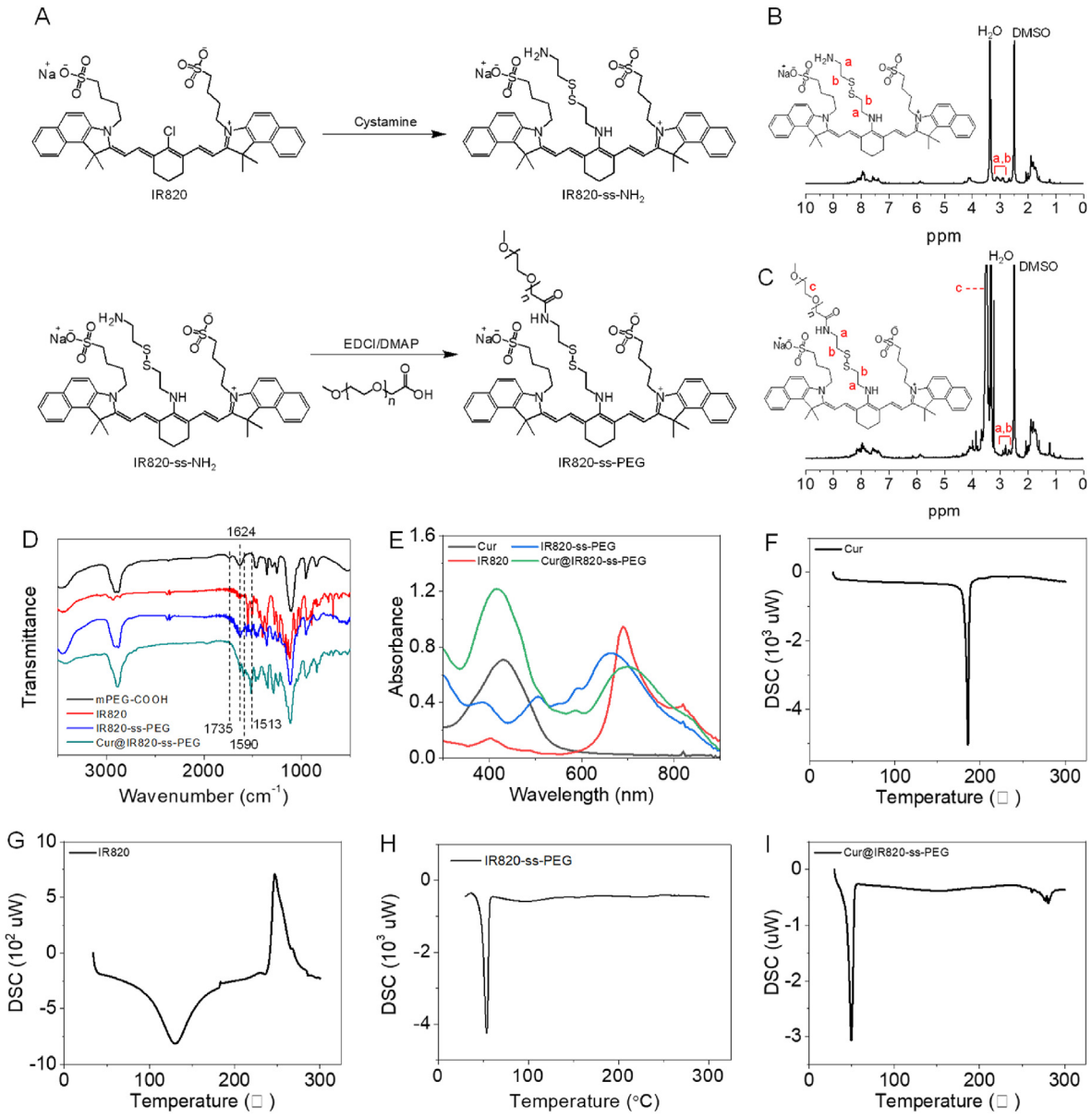

Fig. 1. (A) Synthetic scheme of IR820-ss-PEG. (B) ^{1}H NMR spectrum of IR820-ss-NH_2 in DMSO-D_6. (C) ^{1}H NMR spectrum of IR820-ss-PEG in DMSO-D_6. (D) FT-IR spectra of mPEG-COOH, IR820, IR820-ss-PEG and Cur@IR820-ss-PEG. (E) UV–Vis spectra of curcumin (dissolved in ethanol and diluted with deionized water), IR820, IR820-ss-PEG and Cur@IR820-ss-PEG in aqueous solution. (F–H) DSC thermograms of curcumin, IR820, IR820-ss-PEG and Cur@IR820-ss-PEG.

exhibit limited curcumin and IR820 release in pH 7.4 and pH 5.0 PBS buffer without GSH. In contrast, the curcumin and IR820 release is dramatically enhanced in pH 7.4 and pH 5.0 PBS buffer with 10 mmol/L of GSH. For instance, Cur@IR820-ss-PEG release less than 15% of curcumin and less than 25% of IR820 in pH 7.4 and pH 5.0 PBS buffer without GSH at 96 h, while release over 55% of curcumin and IR820 in pH 7.4 and pH 5.0 PBS buffer with 10 mmol/L of GSH at the same time point. Cur@IR820-ss-PEG exhibit slightly reduced curcumin and IR820 release in pH 5.0 PBS buffer with 10 mmol/L of GSH as compared to in pH 7.4 PBS buffer with 10 mmol/L of GSH, which is ascribed to the reduced reactivity of GSH in the mild acidic conditions. To visualize the GSH-induced nanoparticle disintegration, IR820-ss-PEG and Cur@IR820-ss-PEG were treated with 10 mmol/L of GSH for 24 h and then observed with TEM, Fig. S5. After treatment with 10 mmol/L of GSH for 24 h, both IR820-ss-PEG and Cur@IR820-ss-PEG were cleaved into fragments with random shapes. These results indicate that Cur@IR820-ss-PEG exhibit reduction-responsive drug release behaviors and suggest that Cur@IR820-ss-PEG might effectively release the cargos in the tumor cells while be relatively stable in the blood circulation [49, 50].

The cellular uptake of Cur@IR820-ss-PEG on 4T1 cells was observed with fluorescence microscope. As shown in Fig. 3A, Cur@IR820-ss-PEG exhibit significantly enhanced cellular IR820 (red) and curcumin (green) fluorescence intensities as compared to IR820/curcumin mixture (IR820/Cur) after incubation with 4T1 cells for 2 h or 4 h, suggesting that Cur@IR820-ss-PEG exhibit enhanced cellular uptake amount as compared to IR820/Cur. IR820/Cur exhibit similar cellular IR820 and curcumin fluorescence intensities at 2 h and 4 h, while Cur@IR820-ss-PEG display enhanced cellular IR820 and curcumin fluorescence intensities at 4 h with compared to 2 h, suggesting that the cellular uptake of Cur@IR820-ss-PEG is time-dependent. Different from IR820/Cur, curcumin is mainly co-localized with IR820 in 4T1 cells for Cur@IR820-ss-PEG, suggesting that curcumin is taken up together with the nanoparticles for Cur@IR820-ss-PEG. The intracellular curcumin and IR820

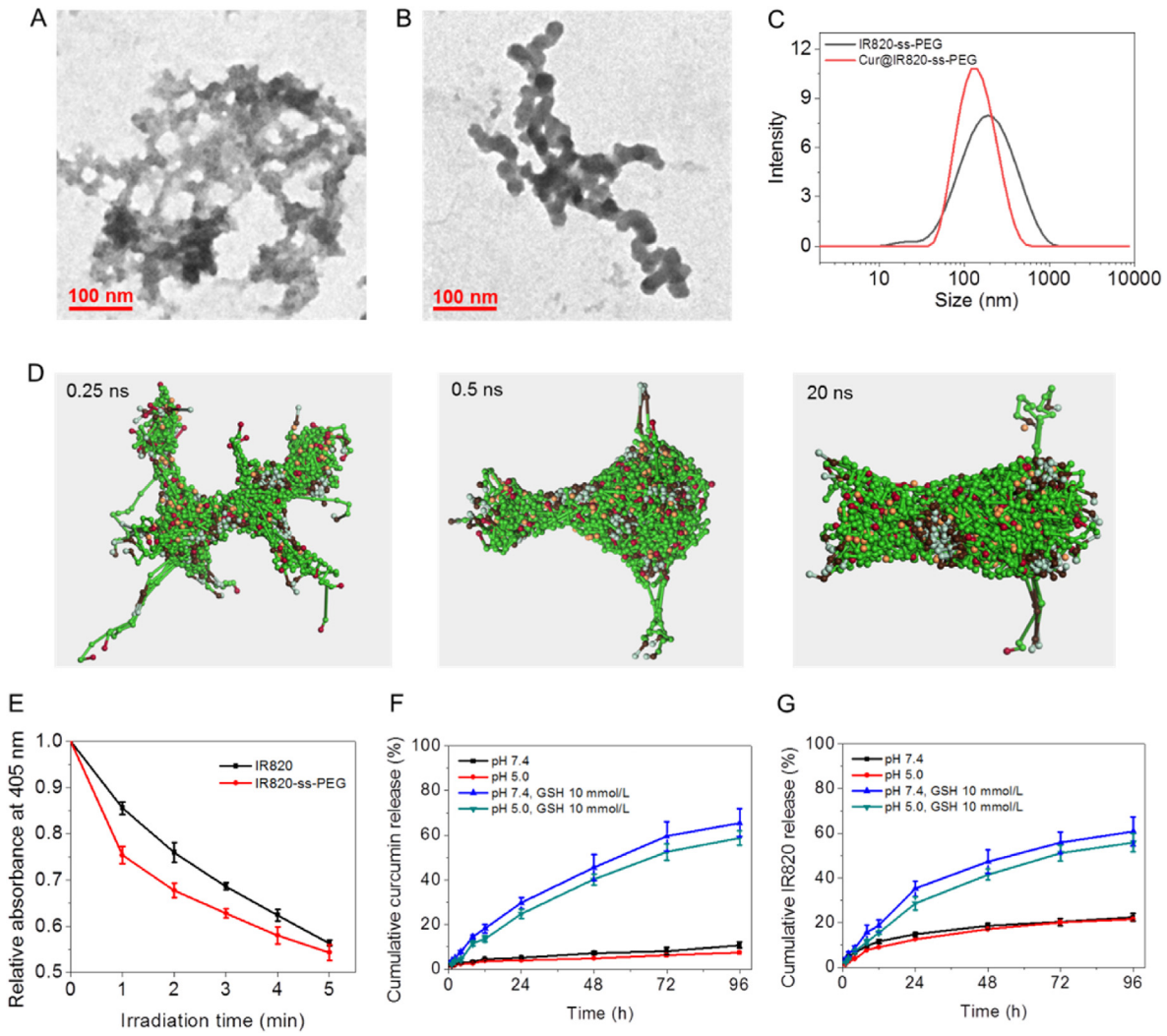

Fig. 2. (A) TEM image of IR820-ss-PEG. (B) TEM image of Cur@IR820-ss-PEG. (C) Size distribution of IR820-ss-PEG and Cur@IR820-ss-PEG determined by DLS. (D) Snapshots of DPD simulation at 0.25 ns, 0.5 ns and 20 ns? (E) Decline of the absorbance of DPBF of each group under 0.5 W/cm^2 660 nm laser irradiation (n = 3). (F) In vitro curcumin release profiles of Cur@IR820-ss-PEG (n = 3). (G) In vitro IR820 release profiles of Cur@IR820-ss-PEG (n = 3).

amount was also determined. As shown in Fig. 3B, Cur@IR820-ss-PEG exhibit 2.0 times higher cellular uptake amount of IR820 and 1.9 times higher cellular uptake amount of curcumin as compared to IR820/Cur at 2 h, while show 3.0 times higher cellular uptake amount of IR820 and 2.4 times higher cellular uptake amount of curcumin as compared to IR820/Cur at 4 h, further confirming the efficient cellular uptake of Cur@IR820-ss-PEG. The efficient cellular uptake of Cur@IR820-ss-PEG might be attributed to their special worm-like morphology, which has higher contact area with cell membranes [51,52]. Considering the short-life time and limited diffusion distance of singlet oxygen generated during PDT, the efficient cellular uptake is essential for potent PDT efficacy [53,54]. Therefore, our prepared worm-like nanoparticles are beneficial for intracellular delivery of IR820 for potent PDT.

The in vitro cytotoxicity against 4T1 cells was evaluated by MTT assays. As shown in Fig. 4A and B, IR820 and IR820-ss-PEG exhibit no significant cytotoxicity against 4T1 cells without laser irradiation, while display dose-dependent cytotoxicity against 4T1 cells with laser irradiation. IR820-ss-PEG show enhanced photocytotoxicity as compared to IR820. IR820/Cur and Cur@IR820-ss-PEG show dose-dependent cytotoxicity against 4T1 cells without laser irradiation and enhanced cytotoxicity against 4T1 cells with laser irradiation. Cur@IR820-ss-PEG exhibit enhanced cytotoxicity against 4T1 cells as compared to IR820/Cur with or without laser irradiation, which is attributed to the efficient cellular uptake and reduction-responsive drug release of Cur@IR820-ss-PEG. To evaluate the combinational therapeutic effect of IR820/Cur and Cur@IR820-ss-PEG, the combinational index was calculated. The combinational index for IR820/Cur and Cur@IR820-ss-PEG was calculated according to Fig. 4B by a Chou-Talalay method [55,56]. As shown in Fig. 4C, the combination index for IR820/Cur are all above 1. In contrast, the combination index for Cur@IR820-ss-PEG are less than 1 when the curcumin concentration is equal to or higher than 2 μg/mL, indicating that curcumin and IR820-ss-PEG in Cur@IR820-ss-PEG exhibit synergistic antitumor effect at relatively high doses. The synergistic chemo-photodynamic antitumor effect of Cur@IR820-ss-PEG is ascribed to their efficient cellular uptake and reduction-triggered drug release. The morphologies of 4T1 cells were observed with microscope to further evaluate the antitumor effect. As shown in Fig. 4D, the shapes of 4T1 cells change significantly for all treatment groups. Cur + Laser group shows certain cell contraction, suggesting that curcumin has chemotherapeutic effect against 4T1 cells. IR820 + Laser group also shows certain cell contraction, suggesting that the photodynamic effect of IR820 induces oxidative stress in 4T1 cells. Compared with Cur + Laser group and IR820 + Laser group, the cell contraction is more apparent in IR820/Cur + Laser group, suggesting that IR820/Cur + Laser exhibit enhanced antitumor effect as compared to Cur + Laser or IR820 + Laser. IR820-ss-PEG + Laser group displays more apparent cell contraction as

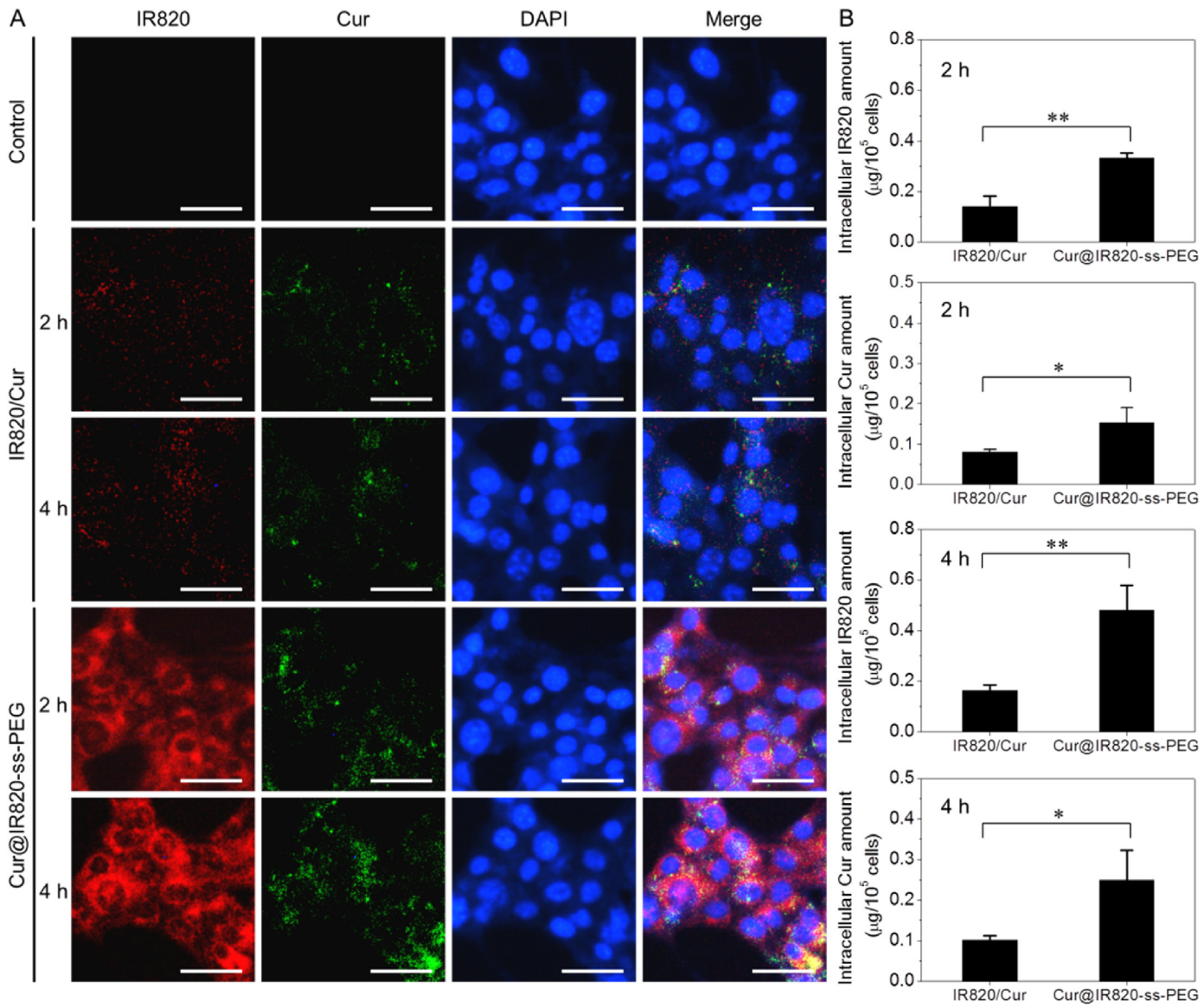

Fig. 3. (A) Cellular uptake of IR820/Cur and Cur@IR820-ss-PEG observed with fluorescence microscope. The scale bar is 50 μm. (B) Cellular uptake amount of IR820 and curcumin for IR820/Cur and Cur@IR820-ss-PEG (n = 3). *$p < 0.05$, **$p < 0.01$.

compared to IR820 + Laser group, suggesting that IR820-ss-PEG exhibit enhanced photodynamic therapeutic effect as compared to IR820. Cur@IR820-ss-PEG + Laser group shows the most apparent cell contraction, indicating that Cur@IR820-ss-PEG + Laser exhibit the most potent antitumor effect. These results are in accordance with the MTT results. To evaluate the photodynamic effect of Cur@IR820-ss-PEG on 4T1 cells, the intracellular ROS level was detected by DCFH-DA [57]. As shown in Fig. 4E and F, IR820/Cur show enhanced intracellular ROS level as compared to non-drug treated cells under laser irradiation and Cur@IR820-ss-PEG exhibit the highest intracellular ROS level under laser irradiation, indicating that Cur@IR820-ss-PEG display enhanced photodynamic effect toward 4T1 cells as compared to IR820/Cur. The in vitro hemolysis study was performed to evaluate the hemo-compatibility of Cur@IR820-ss-PEG. As shown in Fig. 4G, the hemolysis rates of Cur@IR820-ss-PEG are less than 5% in the concentration (IR820) ranging from 10 to 500 μg/mL, indicating that Cur@IR820-ss-PEG possess good hemo-compatibility. Taken together, these results indicate that Cur@IR820-ss-PEG exhibit enhanced in vitro antitumor effect as compared to IR820/Cur as well as good biocompatibility, which are ready for in vivo investigations.

The pharmacokinetics of IR820/Cur and Cur@IR820-ss-PEG were studied on healthy female mice. The mean IR820 plasma concentration-time profiles and mean curcumin plasma concentration-time profiles were shown in Fig. S6 A and B. After intravenous injection, Cur@IR820-ss-PEG exhibit significantly higher IR820 and curcumin plasma concentration as compared to IR820/Cur. The IR820 and curcumin plasma concentration decrease slowly with increasing time for Cur@IR820-ss-PEG, while IR820/Cur display rapid IR820 and curcumin plasma concentration decrease after intravenous injection. The IR820 and curcumin plasma concentration-time profiles are fitted by a three-compartment pharmacokinetic model and the pharmacokinetic parameters were calculated [58,59]. As shown in Table 1, the elimination half-life time ($t_{1/2\gamma}$) of IR820 and curcumin for Cur@IR820-ss-PEG are 9.4 times higher and 3.6 times higher than those for IR820/Cur, the area under curve of IR820 and curcumin for Cur@IR820-ss-PEG are 15.7 times higher and 44.5 times higher than those for IR820/Cur, the volume of distribution (V) and clearance rate (CL) of IR820 and curcumin for Cur@IR820-ss-PEG are significantly lower than those for IR820/Cur. These results indicate that Cur@IR820-ss-PEG exhibit significantly prolonged blood circulation as compared to IR820/Cur. Due to the stealth

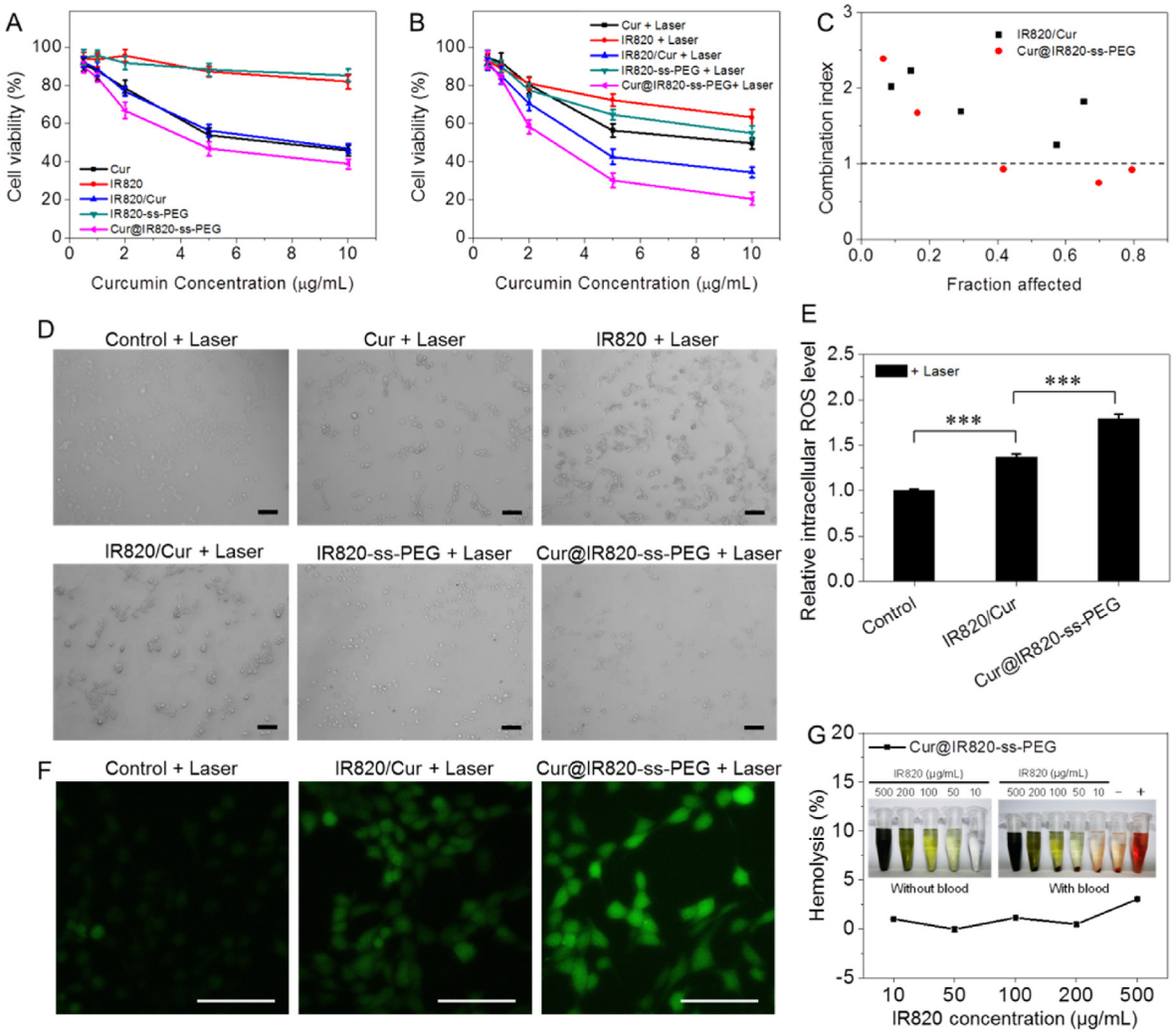

Fig. 4. (A) In vitro cytotoxicity against 4T1 cells without laser irradiation (n = 4). (B) In vitro cytotoxicity against 4T1 cells with 0.5 W/cm^2 660 nm laser irradiation for 3 min (n = 4). (C) Combination index for IR820/Cur and Cur@IR820-ss-PEG. (D) Morphologies of 4T1 cells after different treatment. The scale bar is 100 μm. (E) Intracellular ROS level of 4T1 cells treated with different formulations for 4 h and exposed to 0.5 W/cm^2 660 nm laser irradiation for 3 min (n = 3). (F) Intracellular ROS detected by DCFH-DA. The scale bar is 100 μm. (G) Hemolysis ratio of Cur@IR820-ss-PEG with different concentrations of IR820 (n = 3). $^{**}p < 0.01$, $^{***}p < 0.001$.

Table 1
Average pharmacokinetic parameters of IR820/Cur and Cur@IR820-ss-PEG after intravenous injection to mice (n = 3).

Parameter	IR820		Curcumin	
	IR820/Cur	Cur@IR820-ss-PEG	IR820/Cur	Cur@IR820-ss-PEG
$t_{1/2\gamma}$ (h)	0.327	3.075	0.562	2.030
AUC (0-t) (mg/L* h)	0.938	14.68	0.120	5.344
V (L/kg)	3.634	0.142	14.217	0.393
CL (L/h/kg)	18.412	1.178	136.976	3.236

$t_{1/2\gamma}$, elimination half-life time. AUC, area under curve. V, volume of distribution. CL, clearance rate.

effect of PEG, limited drug release in physiological conditions and relatively small particle size, Cur@IR820-ss-PEG could escape from the capture of the reticuloendothelial system and therefore prolong the blood circulation time of both IR820 and curcumin.

The biodistribution of Cur@IR820-ss-PEG was studied on subcutaneous 4T1 tumor-bearing mice. Cur@IR820-ss-PEG and IR820/Cur were intravenously injected to the tumor-bearing mice. The mice were sacrificed 4 h, 12 h and 24 h after administration and the major organs and tumors were harvested for ex vivo fluorescence imaging. As shown in Fig. 5A and B, the fluorescence of IR820 for Cur@IR820-ss-PEG is mainly distributed in tumor, kidney and lung at 4 h. Cur@IR820-ss-PEG exhibit enhanced tumor and kidney accumulation and reduced lung accumulation at 12 h with compared to 4 h, Fig. 5C and D. At 24 h, Cur@IR820-ss-PEG exhibit reduced accumulation in kidney, but the accumulation of Cur@IR820-ss-PEG in tumor and lung does not change very much, Figure E and F. Different from Cur@IR820-ss-PEG, the fluorescence of IR820 for IR820/Cur is mainly distributed in tumor, kidney and liver at 4 h [60,61]. Compared to 4 h, IR820/Cur exhibit enhanced tumor accumulation and reduced liver and kidney accumulation at 12 h. IR820/Cur exhibit significantly decreased tumor, liver and kidney accumulation and increased lung accumulation at 24 h with compared to 12 h. These results indicate that Cur@IR820-ss-PEG and IR820/Cur have different biodistribution. Cur@IR820-ss-PEG exhibit significantly reduced liver accumulation and enhanced tumor accumulation as compared to IR820/Cur, suggesting that Cur@IR820-ss-PEG might effectively escape from the capture of reticuloendothelial system in liver and preferentially accumulate in tumor by the enhanced permeability and retention effect. Both Cur@IR820-ss-PEG and IR820/Cur exhibit significant accumulation

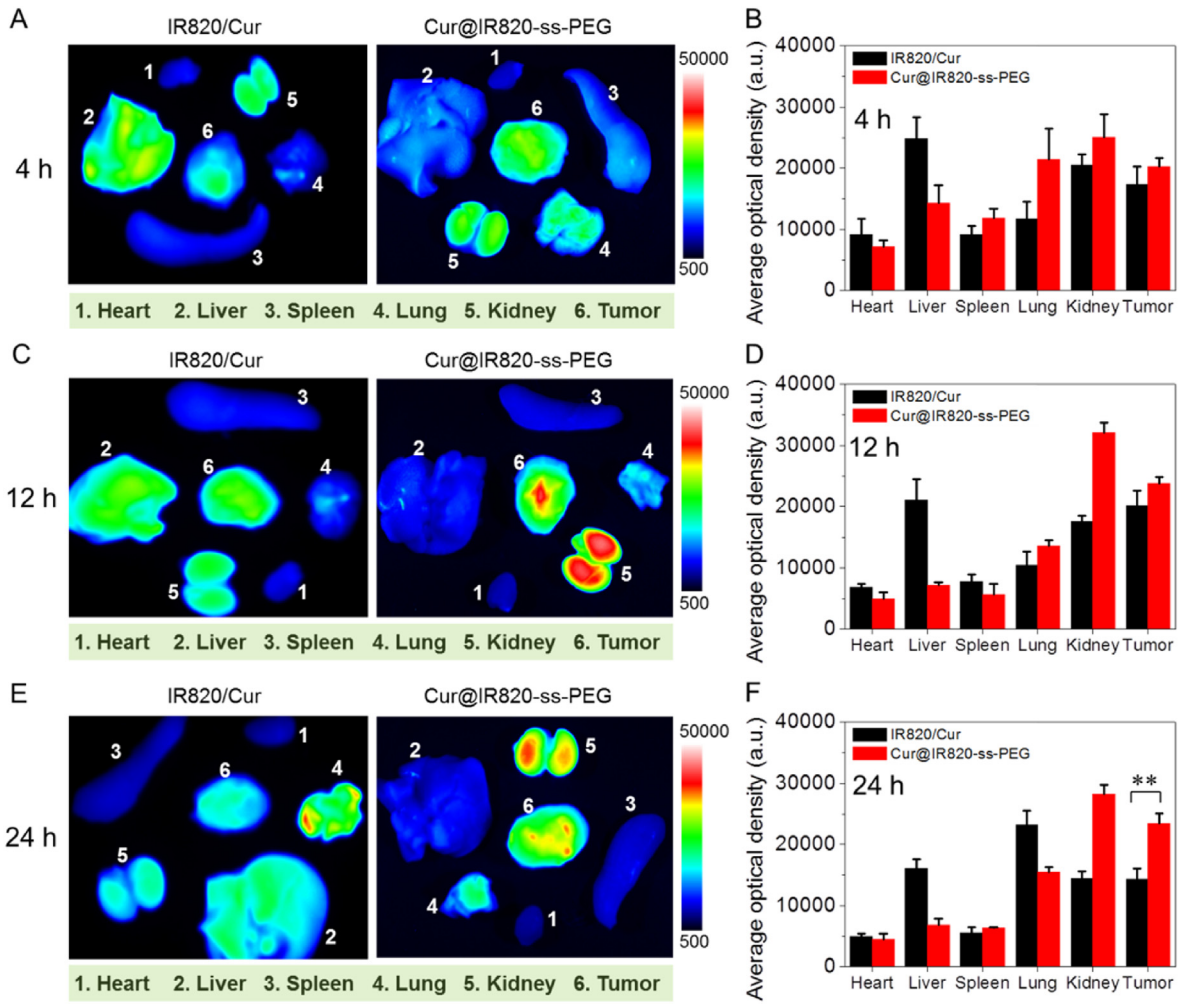

Fig. 5. Representative ex vivo fluorescence images of the major organs and tumors 4 h (A), 12 h (C) and 24 h (E) after intravenous injection of Cur@IR820-ss-PEG and IR820/Cur. Average IR820 fluorescence intensities of organs and tumors 4 h (B), 12 h (D) and 24 h (F) after intravenous injection of Cur@IR820-ss-PEG and IR820/Cur (n = 3). $^{**}p < 0.01$.

in kidney, implying that kidney filtration might be involved in the excretion of IR820. Taken together, these results indicate that Cur@IR820-ss-PEG exhibit enhanced tumor accumulation and retention as compared to IR820/Cur.

Curcumin is reported to decrease HIF-1α protein expression level of tumor cells and suppress the transcriptional activity of HIF-1 under hypoxia, leading to the decrease of the VEGF protein expression level and inhibition of HIF-1α-mediated angiogenesis [30,31]. To evaluate the suppression effect of Cur@IR820-ss-PEG on HIF-1α and VEGF in tumors, subcutaneous 4T1 tumor-bearing mice were intravenously injected with different formulations and the tumor HIF-1α and VEGF protein expression levels of each group were studied by immunofluorescent staining 24 h after intravenous injection. As shown in Fig. 6A and C, IR820/Cur group show significantly decreased tumor HIF-1α and VEGF protein expression levels as compared to PBS group, and Cur@IR820-ss-PEG group display lower tumor HIF-1α and VEGF protein expression levels as compared to IR820/Cur group. These results indicate that Cur@IR820-ss-PEG exhibit enhanced HIF-1α and VEGF suppression effect as compared to IR820/Cur. The enhanced HIF-1α and VEGF suppression effect of Cur@IR820-ss-PEG is attributed to their enhanced tumor accumulation and retention, efficient cellular uptake and reduction-responsive drug release. It has been reported that PDT treatment enhances HIF-1 and VEGF expression in tumor cells, which is beneficial for angiogenesis and might results in the tumor proliferation and subsequent tumor recurrence and metastasis [62]. Accordingly, the tumor HIF-1α and VEGF expression levels after PDT were studied. As shown in Fig. 6B and D, IR820-ss-PEG + Laser group exhibit enhanced HIF-1α and VEGF expression levels as compared to PBS + Laser group, suggesting that the PDT worsens the tumor hypoxia which promotes the expression of VEGF. In contrast, Cur@IR820-ss-PEG + Laser group still exhibit significantly reduced HIF-1α and VEGF expression levels, suggesting that Cur@IR820-ss-PEG effectively suppress tumor HIF-1α and VEGF expression even after PDT. Since HIF-1α/VEGF signaling plays an important role in the resistance against PDT, the efficient suppression effect of Cur@IR820-ss-PEG on H1F-1α and VEGF might inhibit the angiogenesis and increase the apoptosis of tumor cells, which ultimately enhance the chemo-photodynamic therapeutic effect.

The in vivo antitumor effect was studied on subcutaneous 4T1 tumor-bearing mice. Tumor-bearing mice were intravenously injected with different formulations at day 1 and day 3. The mice were irradiated with 0.5 W/cm^2 660 nm laser (3 min) 24 h after administration. As shown in Fig. 7A, both curcumin and IR820 exhibit weak tumor growth inhibition effect, IR820/Cur exhibit slightly enhanced tumor growth inhibition effect as compared to curcumin or IR820, and Cur@IR820-ss-PEG exhibit significantly enhanced tumor growth inhibition effect as compared to IR820/Cur. The tumor inhibition rates of curcumin, IR820, IR820/Cur and Cur@IR820-ss-PEG are 13.9%, 23.2%, 36.0% and 61.8%, respectively. The tumor weight determined at the end of the test shows similar

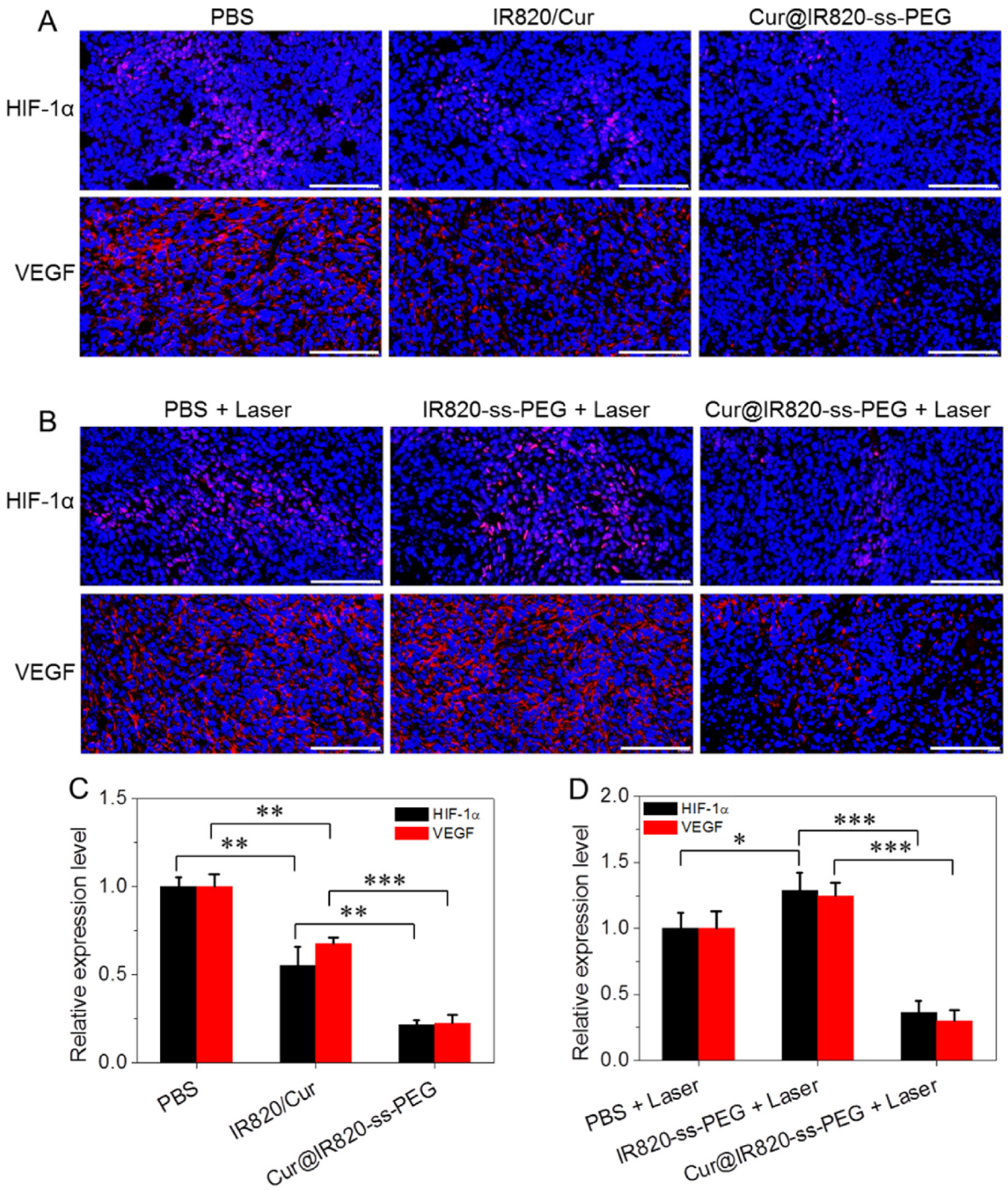

Fig. 6. (A) HIF-1α (pink) and VEGF (red) immunofluorescent staining of tumor sections 24 h after intravenous administration of Cur@IR820-ss-PEG and IR820/Cur. The scale bar is 100 μm. (B) HIF-1α (pink) and VEGF (red) immunofluorescent staining of tumor sections 24 h after laser irradiation. The scale bar is 100 μm. (C) Tumor HIF-1α and VEGF expression level 24 h after intravenous administration of Cur@IR820-ss-PEG and IR820/Cur (n = 3). (D) Tumor HIF-1α and VEGF expression level 24 h after laser irradiation (n = 3). $^{**}p < 0.05$, $^{**}p < 0.01$, $^{***}p < 0.001$. (For interpretation of the references to colour in this figure legend, the reader is referred to the Web version of this article.)

results, Fig. 7B. As shown in Fig. 7C, all treatment groups show no apparent bodyweight changes, suggesting that all tested formulations exhibit good biocompatibility.

The antitumor effect was also evaluated by H & E staining, TUNEL, Ki67 and CD34 immunofluorescent staining of tumor sections. The H & E staining results show that curcumin, IR820 and IR820/Cur groups all display slightly reduced tumor cell density as compared to PBS group and Cur@IR820-ss-PEG group exhibits the lowest tumor cell density, Fig. 7D. The TUNEL immunofluorescent staining results show that both curcumin and IR820 groups display few tumor cell apoptosis, IR820/Cur group exhibits enhanced tumor cell apoptosis ratio (8.8 ± 2.3%) as compared to curcumin group (4.0 ± 1.8%) or IR820 group (5.2 ± 2.5%), and Cur@IR820-ss-PEG group exhibits the highest tumor cell apoptosis ratio (15.5 ± 3.6%), Fig. 7D and E. The Ki67 immunofluorescent staining results show that both curcumin (30.6 ± 5.2%) and IR820 (29.4 ± 4.8%) groups exhibit slightly reduced tumor cell proliferation index as compared to PBS group (37.0 ± 6.3%), IR820/Cur group has lower tumor cell proliferation index (19.8 ± 5.5%), and Cur@IR820-ss-PEG group

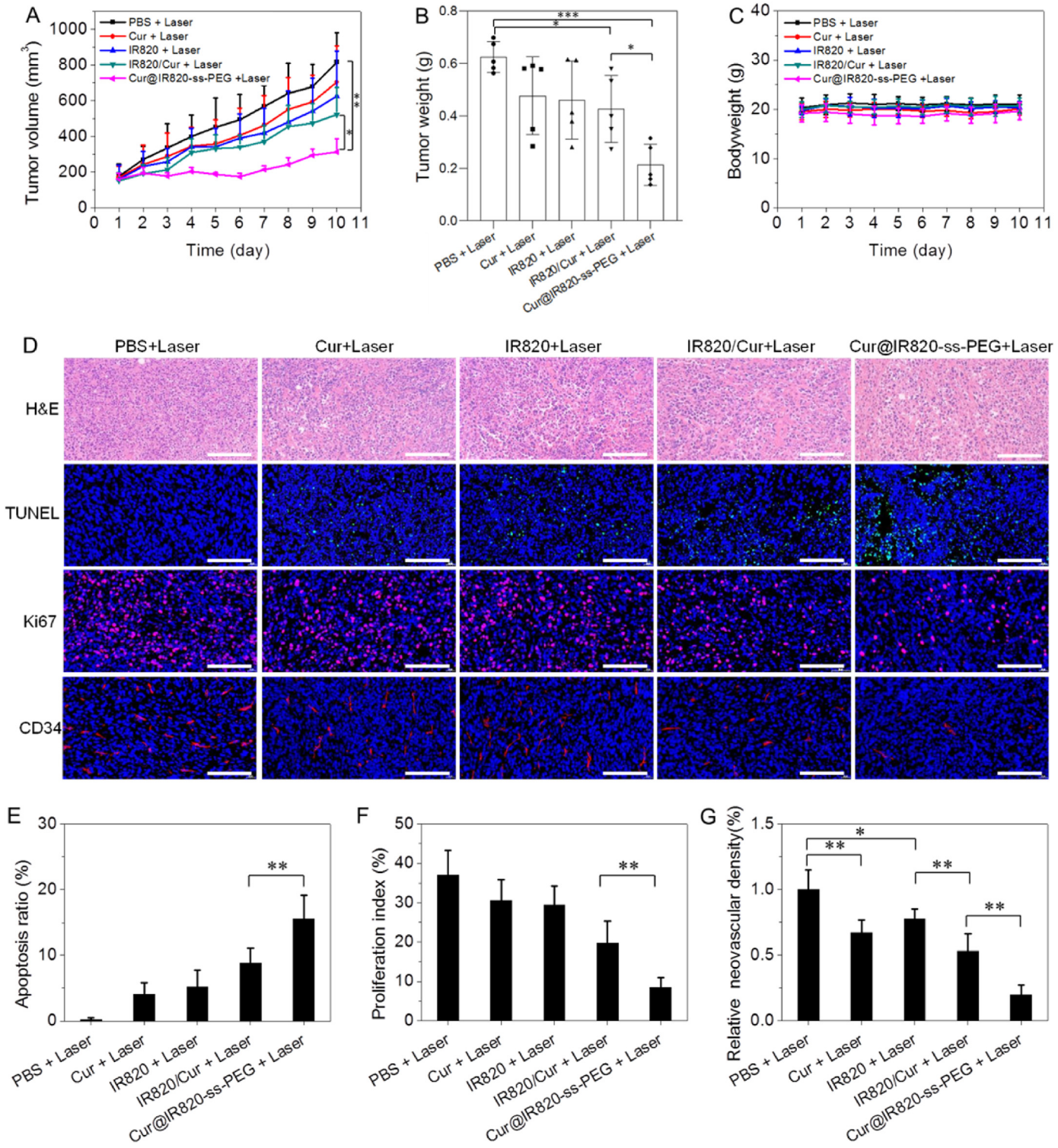

Fig. 7. (A) Tumor volume changes of mice administrated with different formulations and exposed to 0.5 W/cm^2 660 nm laser irradiation (n = 5). (B) Weight of the excised tumors of each group (n = 5). (C) Bodyweight changes of mice from each group (n = 5). (D) H & E staining, TUNEL immunofluorescent staining, Ki67 immunofluorescent staining and anti-CD34 antibody immunofluorescent staining of tumor sections from each group. The scale bar is 100 μm. (E) Apoptosis ratio of tumor cells determined by TUNEL immunofluorescent staining (n = 5). (F) Proliferation index of tumor cells determined by Ki67 immunofluorescent staining (n = 5). (G) Neovascular density of tumors determined by anti-CD34 antibody immunofluorescent staining (n = 5). *$p < 0.05$, **$p < 0.01$, ***$p < 0.001$.

exhibits the lowest tumor cell proliferation index (8.4 ± 2.5%), Fig. 7D and F. These results indicate that Cur@IR820-ss-PEG group exhibits the lowest tumor cell density, highest tumor cell apoptosis ratio and lowest tumor cell proliferation index, further confirming the best antitumor effect of Cur@IR820-ss-PEG. As shown in Fig. 7D and G, the CD34 immunofluorescent staining results show that curcumin, IR820 and IR820/Cur groups all display significantly decreased neovascular density as compared to PBS group and Cur@IR820-ss-PEG exhibit the lowest neovascular density, suggesting that Cur@IR820-ss-PEG effectively inhibit the tumor angiogenesis. The effective inhibition effect of

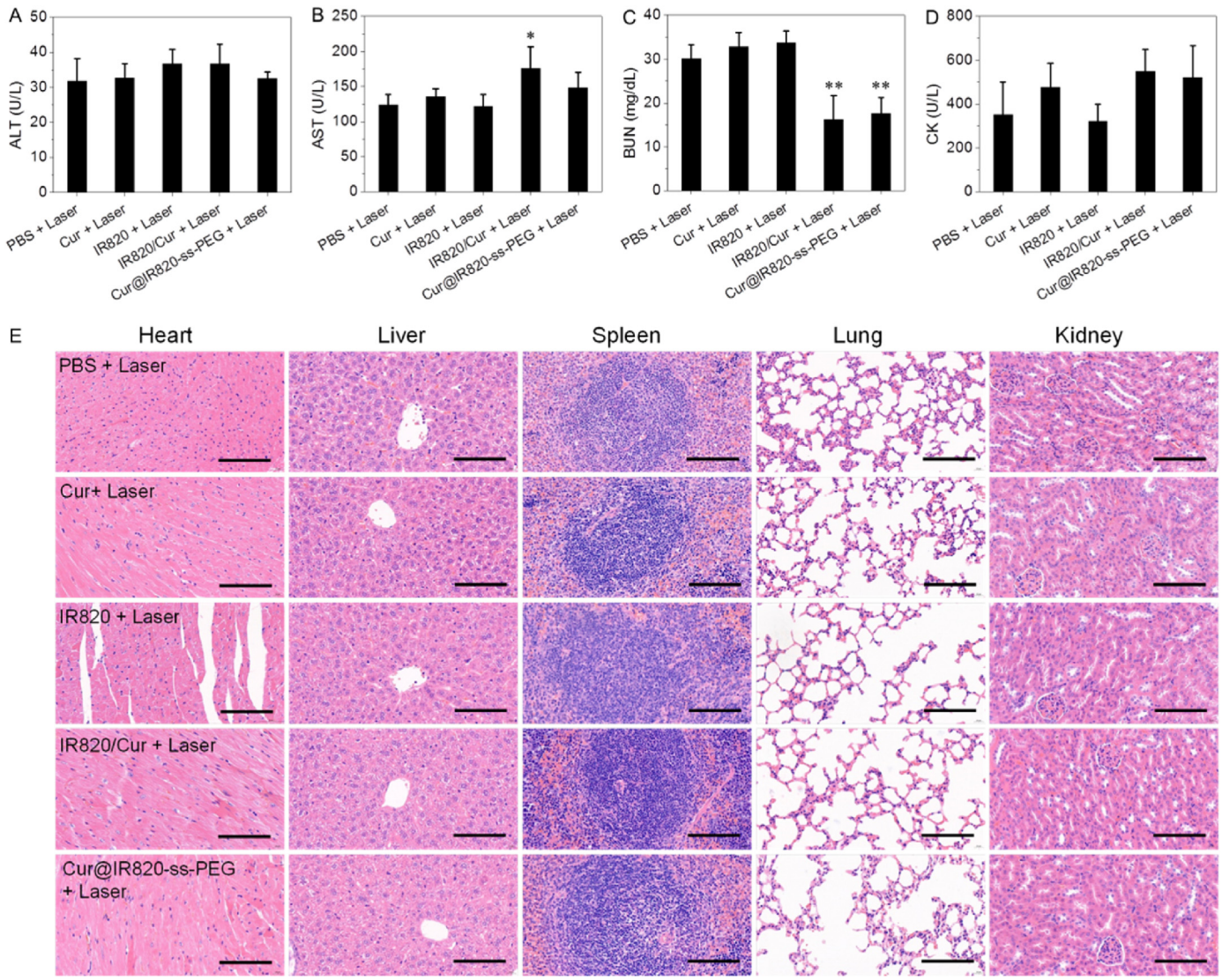

Fig. 8. Serum ALT (A), AST (B), BUN (C) and CK (D) concentrations of each group (n = 5). H & E stained tissue sections of heart, liver, spleen, lung and kidney of mice from each group (E). The scale bar is 100 μm *$p < 0.05$ as compared to PBS + Laser, **$p < 0.01$ as compared to PBS + Laser.

Cur@IR820-ss-PEG on tumor angiogenesis could be ascribed to their efficient suppression effect on H1F-1α and VEGF. H1F-1α/VEGF signaling can induce resistance to PDT through promoting angiogenesis. Therefore, the effective inhibition effect of Cur@IR820-ss-PEG on tumor angiogenesis could boost the PDT efficacy, resulting in the synergistic antitumor effect. Collectively, these results indicate that Cur@IR820-ss-PEG effectively inhibit the tumor angiogenesis, which potentiates the PDT efficacy and leads to the best antitumor effect of Cur@IR820-ss-PEG.

The potential side effects of the tested formulations were studied by blood biochemical analysis and histopathological analysis. To evaluate the function of liver, the serum alanine aminotransferase (ALT) and aspartate aminotransferase (AST) concentrations were measured. The serum blood urea nitrogen (BUN) and creatinine kinase (CK) concentrations were also measured to evaluate the function of kidney and heart, respectively. As shown in Fig. 8 A, all treatment groups exhibit similar serum ALT concentrations as compared to PBS group. Curcumin, IR820 and Cur@IR820-ss-PEG groups show similar serum AST concentrations as compared to PBS group, Fig. 8B. Although the serum AST concentration of IR820/Cur group is significantly higher than PBS group, it is still in the normal range (36–235 U/L). These results suggest that all tested formulations exhibit no significant liver toxicity. Curcumin group and IR820 group exhibit similar serum BUN concentrations as compared to PBS group, Fig. 8C. IR820/Cur group and Cur@IR820-ss-PEG group display significant decreased serum BUN concentrations as compared to PBS group, but they are still in the normal range (11–35 mg/dL). As shown in Fig. 8D, all treatment groups exhibit no significant differences in serum CK concentrations as compared to PBS group, indicating that all tested formulations exhibit no apparent heart toxicity. The H & E stained heart, liver, spleen, lung and kidney sections of all treatment groups exhibit no significant histopathological changes, indicating that all tested formulations exhibit no apparent heart, liver, spleen, lung and kidney toxicity, Fig. 8E. The blood biochemical analysis and histopathological analysis results indicate that all tested formulations exhibit good safety.

4. Conclusion

In summary, Cur@IR820-ss-PEG nanoparticles were developed for synergistic cancer chemo-photodynamic therapy. Cur@IR820-ss-PEG were prepared through a thin-film hydration method and exhibit high drug loading content, worm-like morphology and reduction-responsive drug release. Due to the special worm-like morphology, Cur@IR820-ss-PEG exhibit significantly enhanced cellular uptake efficiency as compared to IR820/Cur, resulting in enhanced in vitro cytotoxicity against 4T1 cells as compared to IR820/Cur under laser irradiation. In

vivo studies, Cur@IR820-ss-PEG exhibit prolonged blood circulation time, enhanced tumor accumulation and retention, improved suppression effect on HIF-1α and VEGF as compared to IR820/Cur. As a consequence, Cur@IR820-ss-PEG significantly inhibit the tumor angiogenesis in vivo antitumor activity study, which potentiates the PDT efficacy and leads to the best in vivo antitumor effect of Cur@IR820-ss-PEG. Cur@IR820-ss-PEG developed in this work provides a novel strategy for synergistic cancer chemo-photodynamic therapy.

Credit author statement

Hang Hu: Conceptualization, Methodology, Software, Formal analysis, Investigation, Writing-Original Draft, Writing-Review & Editing, Visualization, Funding acquisition. **Defeng Xu**: Methodology, Validation, Investigation, Resources, Writing-Review & Editing. **Qingbo Xu**: Investigation, Software, Formal analysis, Funding acquisition, Writing-Review & Editing. **Yuxiang Tang**: Investigation, Resources, Data Curation. **Jun Hong**: Investigation, Software. **Yu Hu**: Conceptualization, Validation, Writing-Review & Editing, Resources. **Jianhao Wang**: Conceptualization, Validation, Resources, Supervision, Writing-Review & Editing. **Xinye Ni**: Conceptualization, Project administration, Validation, Resources, Supervision, Writing-Review & Editing.

Declaration of competing interest

The authors declare that they have no known competing financial interests or personal relationships that could have appeared to influence the work reported in this paper.

Data availability

The authors do not have permission to share data.

Acknowledgements

This work was supported by the grants from the Jiangsu Provincial Outstanding Postdoctoral Program (Grant No. 2022ZB822), Guangdong Basic and Applied Basic Research Foundation (Grant No. 2022A1515010400) and Xiangshan talent project of Zhuhai People's Hospital (Grant No. 2021XSYC-04).

Appendix A. Supplementary data

Supplementary data to this article can be found online at https://doi.org/10.1016/j.mtbio.2023.100542.

References

[1] H. Shi, P.J. Sadler, How promising is phototherapy for cancer? Br. J. Cancer 123 (6) (2020) 871–873.
[2] S.S. Lucky, K.C. Soo, Y. Zhang, Nanoparticles in photodynamic therapy, Chem. Rev. 115 (4) (2015) 1990–2042.
[3] Y. Zhou, X. Ren, Z. Hou, N. Wang, Y. Jiang, Y. Luan, Engineering a photosensitizer nanoplatform for amplified photodynamic immunotherapy via tumor microenvironment modulation, Nanoscale Horiz 6 (2) (2021) 120–131.
[4] M. Zhang, X. Qin, W. Xu, Y. Wang, Y. Song, S. Garg, Y. Luan, Engineering of a dual-modal phototherapeutic nanoplatform for single NIR laser-triggered tumor therapy, J. Colloid Interface Sci. 594 (2021) 493–501.
[5] J. Zhang, N. Wang, Q. Li, Y. Zhou, Y. Luan, A two-pronged photodynamic nanodrug to prevent metastasis of basal-like breast cancer, Chem. Commun. (Camb) 57 (18) (2021) 2305–2308.
[6] X. Qin, M. Zhang, Z. Zhao, Q. Du, Q. Li, Y. Jiang, F. Xue, Y. Luan, A carrier-free photodynamic nanodrug to enable regulation of dendritic cells for boosting cancer immunotherapy, Acta Biomater. 147 (2022) 366–376.
[7] Y. Luo, Y. Song, M. Wang, T. Jian, S. Ding, P. Mu, Z. Liao, Q. Shi, X. Cai, H. Jin, D. Du, W.J. Dong, C.L. Chen, Y. Lin, Bioinspired peptoid nanotubes for targeted tumor cell imaging and chemo-photodynamic therapy, Small 15 (43) (2019), e1902485.
[8] C. Du, Y. Liang, Q. Ma, Q. Sun, J. Qi, J. Cao, S. Han, M. Liang, B. Song, Y. Sun, Intracellular tracking of drug release from pH-sensitive polymeric nanoparticles via FRET for synergistic chemo-photodynamic therapy, J. Nanobiotechnology 17 (1) (2019) 113.
[9] S.S. Panikar, G. Ramirez-Garcia, A.A. Vallejo-Cardona, N. Banu, O.A. Patron-Soberano, D. Cialla-May, T.A. Camacho-Villegas, E. de la Rosa, Novel anti-HER2 peptide-conjugated theranostic nanoliposomes combining NaYF4:Yb,Er nanoparticles for NIR-activated bioimaging and chemo-photodynamic therapy against breast cancer, Nanoscale 11 (43) (2019) 20598–20613.
[10] G. Cheng, W. Zong, H. Guo, F. Li, X. Zhang, P. Yu, F. Ren, X. Zhang, X. Shi, F. Gao, J. Chang, S. Wang, Programmed size-changeable nanotheranostic agents for enhanced imaging-guided chemo/photodynamic combination therapy and fast elimination, Adv. Mater. 33 (21) (2021), e2100398.
[11] Y. Huang, H. Lai, J. Jiang, X. Xu, Z. Zeng, L. Ren, Q. Liu, M. Chen, T. Zhang, X. Ding, C. Zhao, S. Cui, pH-activatable oxidative stress amplifying dissolving microneedles for combined chemo-photodynamic therapy of melanoma, Asian J. Pharm. Sci. 17 (5) (2022) 679–696.
[12] L. Luo, Y. Qi, H. Zhong, S. Jiang, H. Zhang, H. Cai, Y. Wu, Z. Gu, Q. Gong, K. Luo, GSH-sensitive polymeric prodrug: synthesis and loading with photosensitizers as nanoscale chemo-photodynamic anti-cancer nanomedicine, Acta Pharm. Sin. B 12 (1) (2022) 424–436.
[13] Y. Yang, F. Chen, N. Xu, Q. Yao, R. Wang, X. Xie, F. Zhang, Y. He, D. Shao, W.F. Dong, J. Fan, W. Sun, X. Peng, Red-light-triggered self-destructive mesoporous silica nanoparticles for cascade-amplifying chemo-photodynamic therapy favoring antitumor immune responses, Biomaterials 281 (2022), 121368.
[14] Y. Liu, F. Deng, R. Zheng, X. Chen, L. Zhao, B. Yu, A. Chen, X. Jiang, H. Cheng, S. Li, Self-delivery nanomedicine for vascular disruption-supplemented chemo-photodynamic tumor therapy, J. Colloid Interface Sci. 612 (2022) 562–571.
[15] M. Ai, P. Budhani, J. Sheng, S. Balasubramanyam, T. Bartkowiak, A.R. Jaiswal, C.R. Ager, D.D. Haria, M.A. Curran, Tumor hypoxia drives immune suppression and immunotherapy resistance, J. Immunother. Cancer 3 (Suppl 2) (2015) P392.
[16] V. Das, J. Stepankova, M. Hajduch, J.H. Miller, Role of tumor hypoxia in acquisition of resistance to microtubule-stabilizing drugs, Biochim. Biophys. Acta 1855 (2) (2015) 172–182.
[17] M.E. Rodríguez, C. Catrinacio, A. Ropolo, V.A. Rivarola, M.I. Vaccaro, A novel HIF-1α/VMP1-autophagic pathway induces resistance to photodynamic therapy in colon cancer cells, Photoch, Photobio. Sci. 16 (11) (2017) 1631–1642.
[18] A.L. Chédeville, P.A. Madureira, The role of hypoxia in glioblastoma radiotherapy resistance, Cancers 13 (3) (2021) 542.
[19] B. Pucelik, A. Sułek, A. Barzowska, J.M. Dąbrowski, Recent advances in strategies for overcoming hypoxia in photodynamic therapy of cancer, Cancer Lett. 492 (2020) 116–135.
[20] Z. Ji, G. Yang, S. Shahzidi, K. Tkacz-Stachowska, Z. Suo, J.M. Nesland, Q. Peng, Induction of hypoxia-inducible factor-1α overexpression by cobalt chloride enhances cellular resistance to photodynamic therapy, Cancer Lett. 244 (2) (2006) 182–189.
[21] W.H. Chen, R.L. Lecaros, Y.C. Tseng, L. Huang, Y.C. Hsu, Nanoparticle delivery of HIF1alpha siRNA combined with photodynamic therapy as a potential treatment strategy for head-and-neck cancer, Cancer Lett. 359 (1) (2015) 65–74.
[22] Z. Yuan, C. Liu, Y. Sun, Y. Li, H. Wu, S. Ma, J. Shang, Y. Zhan, P. Yin, F. Gao, Bufalin exacerbates Photodynamic therapy of colorectal cancer by targeting SRC-3/HIF-1α pathway, Int. J. Pharma. 624 (2022), 122018.
[23] D. Zheng, C. Huang, H. Huang, Y. Zhao, M.R.U. Khan, H. Zhao, L. Huang, Antibacterial mechanism of curcumin: a review, Chem. Biodiver. 17 (8) (2020), e2000171.
[24] B. Kocaadam, N. Şanlier, Curcumin, an active component of turmeric (Curcuma longa), and its effects on health, Crit. Rev. Food Sci. 57 (13) (2017) 2889–2895.
[25] R.L. Edwards, P.B. Luis, P.V. Varuzza, A.I. Joseph, S.H. Presley, R. Chaturvedi, C. Schneider, The anti-inflammatory activity of curcumin is mediated by its oxidative metabolites, J. Biol. Chem. 292 (52) (2017) 21243–21252.
[26] H. Mirzaei, H. Bagheri, F. Ghasemi, M.J. Khoi, H.M. Pourhanifeh, V.Y. Heyden, E. Mortezapour, A. Nikdasti, P. Jeandet, H. Khan, A. Sahebkar, Anti-cancer activity of curcumin on multiple myeloma, anti-cancer agent, Me 21 (5) (2021) 575–586.
[27] M. Ashrafizadeh, H. Yaribeygi, A. Sahebkar, Therapeutic effects of curcumin against bladder cancer: a review of possible molecular pathways, anti-cancer agent, Me 20 (6) (2020) 667–677.
[28] A.S. Darvesh, B.B. Aggarwal, A. Bishayee, Curcumin and liver cancer: a review, Curr. Pharmaceut. Biotechnol. 13 (1) (2012) 218–228.
[29] K.A. Barcelos, C.R. Mendonça, M. Noll, A.F. Botelho, C.R. Francischini, M.A. Silva, Antitumor properties of curcumin in breast cancer based on preclinical studies: a systematic review, Cancers 14 (9) (2022) 2165.
[30] Z. Cao, S. He, Y. Peng, X. Liao, H. Lu, Nanocurcumin inhibits angiogenesis via down-regulating hif1a/VEGF-A signaling in zebrafish, Curr. Neurovascular Res. 17 (2) (2020) 147–154.
[31] M.-K. Bae, S.-H. Kim, J.-W. Jeong, Y.M. Lee, H.-S. Kim, S.-R. Kim, I. Yun, S.-K. Bae, K.-W. Kim, Curcumin inhibits hypoxia-induced angiogenesis via down-regulation of HIF-1, Oncol. Rep. 15 (6) (2006) 1557–1562.
[32] B. Shan, C. Schaaf, A. Schmidt, K. Lucia, M. Buchfelder, M. Losa, D. Kuhlen, J. Kreutzer, M.J. Perone, E. Arzt, G.K. Stalla, U. Renner, Curcumin suppresses HIF1A synthesis and VEGFA release in pituitary adenomas, J. Endocrinol. 214 (3) (2012) 389–398.
[33] X. Dong, R.K. Brahma, C. Fang, S.Q. Yao, Stimulus-responsive self-assembled prodrugs in cancer therapy, Chem. Sci. 13 (15) (2022) 4239–4269.
[34] M.J. Mitchell, M.M. Billingsley, R.M. Haley, M.E. Wechsler, N.A. Peppas, R. Langer, Engineering precision nanoparticles for drug delivery, Nat. Rev. Drug Discov. 20 (2) (2021) 101–124.
[35] J.K. Patra, G. Das, L.F. Fraceto, E.V.R. Campos, M.d.P. Rodriguez-Torres, L.S. Acosta-Torres, L.A. Diaz-Torres, R. Grillo, M.K. Swamy, S. Sharma,

S. Habtemariam, H.-S. Shin, Nano based drug delivery systems: recent developments and future prospects, J. Nanobiotechnol. 16 (1) (2018) 71.
[36] S. Wilhelm, A.J. Tavares, Q. Dai, S. Ohta, J. Audet, H.F. Dvorak, W.C.W. Chan, Analysis of nanoparticle delivery to tumours, Nat. Rev. Mater. 1 (5) (2016), 16014.
[37] S. Bai, L.-L. Yang, Y. Wang, T. Zhang, L. Fu, S. Yang, S. Wan, S. Wang, D. Jia, B. Li, P. Xue, Y. Kang, Z.-J. Sun, Z. Xu, Prodrug-Based versatile nanomedicine for enhancing cancer immunotherapy by increasing immunogenic cell death, Small 16 (19) (2020), 2000214.
[38] G. Li, B. Sun, Y. Li, C. Luo, Z. He, J. Sun, Small-molecule prodrug nanoassemblies: an emerging nanoplatform for anticancer drug delivery, Small 17 (52) (2021), 2101460.
[39] M. Hou, Y.-E. Gao, X. Shi, S. Bai, X. Ma, B. Li, B. Xiao, P. Xue, Y. Kang, Z. Xu, Methotrexate-based amphiphilic prodrug nanoaggregates for co-administration of multiple therapeutics and synergistic cancer therapy, Acta Biomater. 77 (2018) 228–239.
[40] J. Guan, Y. Wu, H. Wang, H. Zeng, Z. Li, X. Yang, A DiR loaded tumor targeting theranostic cisplatin-icodextrin prodrug nanoparticle for imaging guided chemo-photothermal cancer therapy, Nanoscale 13 (46) (2021) 19399–19411.
[41] H. Cai, P. Tan, X. Chen, M. Kopytynski, D. Pan, X. Zheng, L. Gu, Q. Gong, X. Tian, Z. Gu, H. Zhang, R. Chen, K. Luo, Stimuli-Sensitive linear–dendritic block copolymer–drug prodrug as a nanoplatform for tumor combination therapy, Adv. Mater. 34 (8) (2022), 2108049.
[42] X. Yuan, Y. Tao, W. Xiao, K. Du, H. Hu, D. Xu, Q. Xu, Conjugates of lactobionic acid and IR820: new photosensitizers for efficient photodynamic therapy of hepatoma cells, Drug Dev. Res. 83 (3) (2022) 646–658.
[43] S. Srinivasan, R. Manchanda, A. Fernandez-Fernandez, T. Lei, A.J. McGoron, Near-infrared fluorescing IR820-chitosan conjugate for multifunctional cancer theranostic applications, J. Photochem. Photobiol., B 119 (2013) 52–59.
[44] X. Cui, K. Du, X. Yuan, W. Xiao, Y. Tao, D. Xu, H. Hu, A comparative study of the in vitro antitumor effect of mannose-doxorubicin conjugates with different linkers, Drug Dev. Res. 83 (3) (2022) 646–658.
[45] M. Wang, Y. Lin, J. Gao, D. Liu, DPD simulations on morphologies and structures of blank PLGA-b-PEG-b-PLGA polymeric micelles and docetaxel-loaded PLGA-b-PEG-b-PLGA polymeric micelles, RSC Adv. 12 (19) (2022) 12078–12088.
[46] T. Wei, C. Ren, Chapter 6 - theoretical simulation approaches to polymer research, in: M.A.A. AlMaadeed, D. Ponnamma, M.A. Carignano (Eds.), Polymer Science and Innovative Applications, Elsevier, 2020, pp. 207–228.
[47] H. Hu, X. Liu, J. Hong, N. Ye, C. Xiao, J. Wang, Z. Li, D. Xu, Mesoporous polydopamine-based multifunctional nanoparticles for enhanced cancer phototherapy, J. Colloid Interface Sci. 612 (2022) 246–260.
[48] X. He, J. Hong, S. Liu, D. Xu, H. Hu, Hydroxyethyl starch-new indocyanine green conjugates for enhanced cancer photodynamic therapy, Carbohydr. Res. 508 (2021), 108416.
[49] Y. Li, H. Hu, Q. Zhou, Y. Ao, C. Xiao, J. Wan, Y. Wan, H. Xu, Z. Li, X. Yang, α-Amylase- and redox-responsive nanoparticles for tumor-targeted drug delivery, ACS Appl. Mater. Interfaces 9 (22) (2017) 19215–19230.
[50] H. Hu, Y. Li, Q. Zhou, Y. Ao, C. Yu, Y. Wan, H. Xu, Z. Li, X. Yang, Redox-Sensitive hydroxyethyl starch–doxorubicin conjugate for tumor targeted drug delivery, ACS Appl. Mater. Interfaces 8 (45) (2016) 30833–30844.
[51] Z. Zhang, C. Liu, C. Li, W. Wu, X. Jiang, Shape Effects of Cylindrical versus Spherical Unimolecular Polymer Nanomaterials on in Vitro and in Vivo Behaviors, vol. 2019, Research (Wash D C), 2019, 2391486.
[52] H. Hu, C. Wang, R. Zhang, C. Xiao, C. Lai, Z. Li, D. Xu, Branched worm-like nanoparticles featured with programmed drug release for synergistic castration-resistant prostate cancer therapy, J. Mater. Sci. 55 (16) (2020) 6992–7008.
[53] Z. Yu, W. Pan, N. Li, B. Tang, A nuclear targeted dual-photosensitizer for drug-resistant cancer therapy with NIR activated multiple ROS, Chem. Sci. 7 (7) (2016) 4237–4244.
[54] Z. Yu, Q. Sun, W. Pan, N. Li, B. Tang, A near-infrared triggered nanophotosensitizer inducing domino effect on mitochondrial reactive oxygen species burst for cancer therapy, ACS Nano 9 (11) (2015) 11064–11074.
[55] T.-C. Chou, Theoretical basis, experimental design, and computerized simulation of synergism and antagonism in drug combination studies, pharma, Rev 58 (3) (2006) 621.
[56] H. Hu, D. Xu, Co-delivery of docetaxel and retinoic acid by poly (ethylene glycol)-retinoic acid conjugates based micelles for synergistic prostate cancer therapy, Micro & Nano Lett. 16 (6) (2021) 336–343.
[57] H. Hu, J. Chen, H. Yang, X. Huang, H. Wu, Y. Wu, F. Li, Y. Yi, C. Xiao, Y. Li, Y. Tang, Z. Li, B. Zhang, X. Yang, Potentiating photodynamic therapy of ICG-loaded nanoparticles by depleting GSH with PEITC, Nanoscale 11 (13) (2019) 6384–6393.
[58] Y. Zhang, J. Lv, P. Liu, X. Zhao, K. Chen, Q. Li, L. Nie, C. Fang, Contrast-enhanced multispectral photoacoustic imaging for irregular hepatectomy navigation: a pilot study, ACS Biomater. Sci. Eng. 6 (10) (2020) 5874–5885.
[59] G.T. Bolger, A. Licollari, A. Tan, R. Greil, B. Vcelar, S. Greil-Ressler, L. Weiss, C. Schonlieb, T. Magnes, B. Radl, M. Majeed, P.P. Sordillo, Pharmacokinetics of liposomal curcumin (Lipocurc) infusion: effect of co-medication in cancer patients and comparison with healthy individuals, Cancer Chemother, Pharmacol 83 (2) (2019) 265–275.
[60] A. Fernandez-Fernandez, R. Manchanda, D.A. Carvajal, T. Lei, S. Srinivasan, A.J. McGoron, Covalent IR820-PEG-diamine nanoconjugates for theranostic applications in cancer, Int. J. Nanomedicine 9 (2014) 4631–4648.
[61] K. Huang, M. Gao, L. Fan, Y. Lai, H. Fan, Z. Hua, IR820 covalently linked with self-assembled polypeptide for photothermal therapy applications in cancer, Biomater. Sci. 6 (11) (2018) 2925–2931.
[62] Q. Zhan, W. Yue, S. Hu, Effect of photodynamic therapy and endostatin on human glioma xenografts in nude mice, Photodiagnosis Photodyn. Ther. 8 (4) (2011) 314–320.